OAK RIDGE
NATIONAL LABORATORY
MANAGED BY UT-BATTELLE
FOR THE DEPARTMENT OF ENERGY

ORNL/TM-2009/87

Design Study for a Low-Enriched Uranium Core for the High Flux Isotope Reactor, Annual Report for FY 2008

March 2009

Prepared by
R. T. Primm III
D. Chandler
G. Ilas
B. C. Jolly
J. H. Miller
J. D. Sease

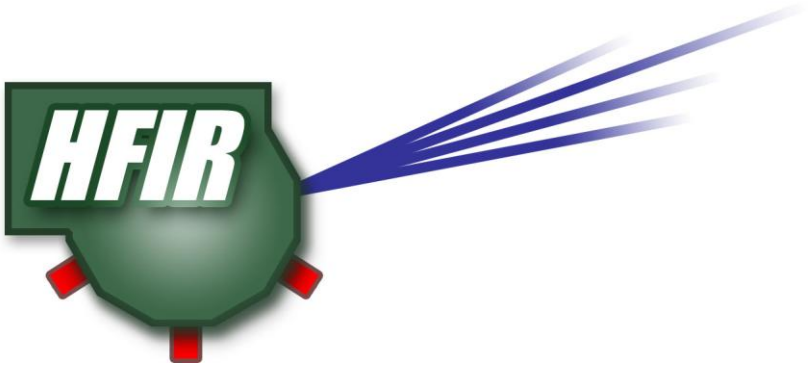

UT-BATTELLE
ORNL-27 (4-00)

ORNL/TM-2009/87

DESIGN STUDY FOR A LOW-ENRICHED URANIUM CORE FOR THE HIGH FLUX ISOTOPE REACTOR, ANNUAL REPORT FOR FY 2008

R. T. Primm III
D. Chandler
G. Ilas
B. C. Jolly
J. H. Miller
J. D. Sease
Oak Ridge National Laboratory

Date Published: March 2009

Prepared by
OAK RIDGE NATIONAL LABORATORY
Oak Ridge, Tennessee 37831-6283
managed by
UT-BATTELLE, LLC
for the
U.S. DEPARTMENT OF ENERGY
under contract DE-AC05-00OR22725

CONTENTS

Page

LIST OF FIGURES

Figure **Page**

LIST OF FIGURES (cont'd)

Figure **Page**

LIST OF TABLES

ACKNOWLEDGMENTS

The authors would like to acknowledge that the support for this project was provided by the Global Threat Reduction Initiative, Reduced Enrichment for Research and Test Reactors Program (RERTR), Nuclear National Security Administration, U.S. Department of Energy (DOE). The DOE program manager, Parrish Staples, Idaho National Laboratory RERTR fuels program manager, Daniel Wachs, and Argonne National Laboratory RERTR reactor analysis program manager, Jim Matos, all provided useful comments and reviews of this work during the fiscal year. The authors also acknowledge the technical reviews of this document preformed by K. A. Smith, Research Reactors Division, and Brian D. Murphy, Nuclear Science and Technology Division, Oak Ridge National Laboratory and thank all of the reviewers for their efforts and comments. Finally, the authors wish to thank Mary Wells for document preparation and editing of this report.

OTHER REPORTS IN THIS SERIES

R. T. Primm III, R. J. Ellis, J. C. Gehin, D. L. Moses, J. L. Binder, and N. Xoubi, *Assumptions and Criteria for Performing a Feasibility Study of the Conversion of the High Flux Isotope Reactor Core to Use Low-Enriched Uranium Fuel*, ORNL/TM-2005/269, February 2006.

R. T. Primm III, R. J. Ellis, J. C. Gehin, K. T. Clarno, K. A. Williams, and D. L. Moses, *Design Study for a Low-Enriched Uranium Core for the High Flux Isotope Reactor, Annual Report for FY 2006,* ORNL/TM-2006/136, November 2006.

J. D. Sease, R. T. Primm III, and J. H. Miller, *Conceptual Process for the Manufacture of Low-enriched Uranium/Molybdenum Fuel for the High Flux Isotope Reactor*, ORNL/TM-2007/39, September 2007.

R. T. Primm III, R. J. Ellis, J. C. Gehin, G. Ilas, J. H. Miller, and J. D. Sease, *Design Study for a Low-Enriched Uranium Core for the High Flux Isotope Reactor, Annual Report for FY 2007,* ORNL/TM-2007/45, November 2007.

D. Chandler, R. T. Primm, III, and G. I. Maldonado, *Validating MCNP for LEU Fuel Design via Power Distribution Comparisons*, ORNL/TM-2008/126, November 2008.

Lee Tschaepe, Arthur E. Ruggles, James D. Freels, and R. T. Primm, III, *Evaluation of HFIR LEU Fuel Using the COMSOL Multiphysics Platform,* ORNL/TM-2008/188, March 2009.

C. Galvez Velit, R. T. Primm III, and J. C. Gehin, *Partial Safety Analysis for a Reduced Uranium Enrichment Core for the High Flux Isotope Reactor,* ORNL/TM-2007/226, April 2009.

ABSTRACT

This report documents progress made during FY 2008 in studies of converting the High Flux Isotope Reactor (HFIR) from high enriched uranium (HEU) fuel to low-enriched uranium (LEU) fuel. Conversion from HEU to LEU will require a change in fuel form from uranium oxide to a uranium-molybdenum alloy. With axial and radial grading of the fuel foil and an increase in reactor power to 100 MW, calculations indicate that the HFIR can be operated with LEU fuel with no degradation in reactor performance from the current level. Results of selected benchmark studies imply that calculations of LEU performance are accurate. Scoping experiments with various manufacturing methods for forming the LEU alloy profile are presented.

1. INTRODUCTION

Design studies for a low-enriched uranium (LEU) core for the High Flux Isotope Reactor (HFIR) were conducted according to the plan documented in Ref. 1. Lists of the studies that had been planned for fiscal year (FY) 2008—published in ref. 1—are shown in Tables 1.1 and 1.2. Those areas in which progress was made and documentation provided in this report are designated by shading. Progress in reactor analysis studies and material development are presented in separate sections of this report. The final section of this report is devoted to a discussion of tasks planned for FY 2009.

Table 1.1. Reactor analysis activities proposed for FY 2008

	Task ID	Subtask description
Reference U-10Mo fuel design	Neutronics	Determine reference, monolithic, 2-D grading profile; steady-state parameters
		Transient analyses of reference design
	Thermal hydraulics	Use newly developed methodology to identify safety margin for reference fuel design
Methods/model development	Cross section processing and deterministic methods completion	Develop/examine 2-D SCALE model
		Transport methods (ATTILA model)
	MCNP model development	Update/make operational MCNP depletion model
	Multidimensional, steady state heat transfer model; turbulent mixing, incorporate diffusion barrier and nonbond assumptions in thermal-hydraulic model	Development of COMSOL based methodology
	Probabilistic combination of uncertainties (if funding is available)	Review/update TASHA code developed under Advanced Neutron Source Program
Program management		Report preparation Travel Review committees
Preparation for regulatory review (if funding is available)		Research publications for LEU validation; develop plan for LEU validation studies
Economic/ engineering assessment (if funding is available)	Conversion to 100 MW	Similar study as Chap. 4 of ref. 2 but identifies cost/schedule for increasing HFIR power so performance meets/exceeds current value

Table 1.2. Fuels development activities proposed for FY 2008

Task name	Comment
Graded fuel development program	Continue grading profile studies with grinding/machining methods. As requested by DOE, collaboration with FRM reactor staff and FRM fuel fabricator (CERCA/ARIVA) on processes for fabricating monolithic fuel
Development of HFIR-specific fuel qualification plan	Issue ORNL/TM by end of fiscal year (included here)
Fuels program management	Includes support to review committees, meeting attendance, travel, and report preparation

2. REACTOR ANALYSES

Both steady-state and time dependent analyses were investigated during FY 2008. Topical reports for some of the analyses have been issued and for those instances, only a limited discussion of the principal conclusions is included in this report. Where investigations are only partially completed or where documentation is incomplete, detailed discussions of the analyses are included as appendices in this report.

Equally important to reactor design are thermal hydraulic methods. During FY08, studies were initiated with three dimensional, finite element based methods with the goal of replacing the capabilities available from an existing, one dimensional conduction computer program[3]. Comparison of modern and currently-accepted thermal hydraulic methods is complicated by the observation that the currently-accepted HFIR methods were written to calculate bounding operating parameters, i.e. safety limits, rather than predicting actual operating conditions or replicating benchmark experiments.

2.1 Steady-State Neutronics Studies

During FY 2008, neutronics analyses evolved from existing, diffusion/depletion based methodology (the VENTURE[4] computer code system) to Monte Carlo/depletion methods (the ALEPH[5] computer code system). While more computationally intensive (time consuming), the accuracy of Monte Carlo methods, especially at interfaces between materials, is unmatched by any other technique. This new Monte Carlo/depletion method has been validated with a measured beginning-of-life power distribution, a measured, simulated end-of-life power distribution, and the core configuration and cycle length for a recent HFIR fuel cycle (cycle number 400)[9]. The methodology was then used to refine the design of the LEU foil fuel that has been described in previous annual reports[1, 2].

2.1.1 Benchmark experiment measurements and calculations

The LEU fuel proposed for HFIR – U-10Mo foils clad in aluminum – has never been used in a reactor nor have any critical experiments been performed with HFIR-typical LEU fuel plates. All of the design effort for HFIR LEU fuel is based on computer simulations. Consequently, it is imperative that methods used to design the LEU fuel be benchmarked with the best available measurements that are representative of expected HFIR conditions with LEU fuel.

Previous annual reports have included analyses documenting that an LEU fuel cycle in HFIR must operate at a higher power and therefore higher power density than the current HEU core. An increase in power of 18% is anticipated. Certifying that the proposed LEU design satisfies existing safety margins requires that the spatially dependent power profile in the reactor be well-known. The level of accuracy with which the reactor power distribution can be calculated is discussed in Appendix A. The conclusion of those studies was that for HFIR HEU fuel, the agreement between calculated and measured local power densities is within the uncertainty of the experimental measurement.

Maintaining reactor performance subsequent to conversion to LEU fuel requires maintaining the same operating cycle length as with the current, HEU fuel cycle. Thus the estimate of cycle length with the new fuel must be shown to be accurate. End-of-life burnup (i.e., cycle length) is reasonably well-calculated with diffusion/depletion methods (ref. 6 with corrections for file limitations in VENTURE) though end-of-life power profiles have questionable accuracy for the bottom of the reactor core. Monte Carlo depletion methodology based on the MCNP models provides the best method for estimating cycle length and, consequently, required beginning-of-life fuel loading.

The ALEPH/MCNP methodology was benchmarked to a recent HFIR (HEU) operating cycle — cycle number 400. The results of the study are presented in Appendix B. The conclusion of the studies was that ALEPH/MCNP "perfectly" predicted the cycle length for HFIR cycle 400.

2.1.2 LEU fuel design

The availability of the ALEPH/MCNP methodology and the confidence inspired in that methodology through the benchmark studies reported in Appendices A and B led to the adoption of that methodology as the "reference" method for designing the LEU fuel cycle. Models of an LEU-fuelled HFIR, developed with the older diffusion/depletion methodology and documented in previous annual reports, were re-examined with the ALEPH methodology. The ALEPH model development is documented in Appendix C.

Expected core LEU loading derived from the older diffusion/depletion methodology was determined to be too low to meet the cycle length reached by the current, HEU fuel cycle. Studies of the relationship between fissile loading and cycle length are presented in Appendix D. The conclusion of those studies is that the ^{235}U loading for a HFIR LEU core to achieve the same performance as the current HEU core is 25.3 kg (HEU core ^{235}U loading is 9.4 kg). The corresponding total uranium loading for an enrichment level of 19.75% is 128.1 kg (HEU core uranium loading is 10.1 kg).

Previous annual reports have documented the observation that power peaking at the top and bottom of the reactor core fuelled with LEU is more severe than for the current, HEU cycle. Such peaking, if not mitigated, would prevent the operation of HFIR with LEU at a power level needed to maintain the current level of performance for the reactor. One method of alleviating the axial power peak in the LEU foil design is to reduce the thickness of the fuel on the ends of the foils, termed axial grading. Scoping calculations had indicated that reducing the foil thickness by 50% over the top and bottommost 2.5 cm would eliminate the flux/power peak and permit reactor operation at 100 MW with LEU fuel. During FY08, studies were performed to determine an optimal, axial grading profile. These studies are still underway but results to date indicate that the length of the axially graded region need not be any longer than 3 cm. The axial grading studies performed in FY08 are presented in Appendix E.

2.1.3 Maintaining independent computational methodology — multidimensional cross section processing

The success with the Monte Carlo/depletion methodology might lead one to conclude that there is no longer a use for currently-accepted, deterministic methods. Three observations justify the maintenance and continued development of deterministic methods. For quality assurance, especially for costly and time consuming projects, a second, independent computational method should be used to verify conclusions drawn from the primary method of analysis. By their nature, deterministic methods may be preferable for calculating small perturbations in physics parameters. Finally, deterministic methods may be preferable for those investigations where an understanding of the spatial and/or energy dependence of parameters are to be inexpensively determined from a single execution of a program. For these reasons development of improved nuclear data processing methods was conducted during FY 2008. The work is described in Appendix F. An assessment of the improvement in the accuracy of ORNL's currently-accepted method, VENTURE, is provided in Appendix G.

The new data-processing technique improves the accuracy of local power density calculations — with the MCNP Monte Carlo calculation taken as the standard per results reported in Section 2.1.1. However the differences between bottom-of-core local power densities between VENTURE and MCNP remain sufficiently large such that ALEPH will continue to be used as the principal design computer program.

2.2 Analyses of Reactor Transients

Studies instigated in 2007 were continued this year. Two transients, a reduction in primary coolant flow and a control element ejection accident, were modeled for both the current HEU fuel cycle and for a prototypic LEU fuel design. Both the primary pump failure transient and the control element ejection transient, each with LEU fuel, were found to have consequences that were comparable to the current HEU fuel cycle.

2.3 Multiphysics Methods Development in Support of Simplier LEU Fuel Designs

Tapering the HFIR LEU foil thickness in the axial direction – top and bottom of the plate – adds a manufacturing process not present in the current, HEU fabrication line. Since axial tapering has never been performed with plate-type fuel and since a goal of the RERTR program is to minimize any change in fabrication cost, eliminating the axial grading step in the fabrication process is an appropriate area for study.

Currently-utilized thermal hydraulic analysis methods for HFIR only account for thermal conduction through the plate surface to the water coolant. Heat conduction along the fuel plate, both axially and along the width of the plate, is not included in the computational models. Turbulent mixing of the water coolant is also not included in the model. Given that the needed improvement in thermal margin is small – the reactor currently operates at 85 MW with HEU and an operating power of 100 MW is proposed for LEU – inclusion of these physical phenomena in the computational methods will provide a more accurate estimate of the safety margin for reactor operation and certainly the newly-estimated margin will be larger than the value that has already been judged acceptable. Hence improvement in computational methods may mitigate the need for axial grading.

Based on prior experience of the HFIR staff, the commercial finite element solver package, COMSOL, was selected as the basis for advancing thermal hydraulics methodology. A series of studies was conducted and are documented in Ref. 18. While studies will continue in FY 2009, it was determined that COMSOL was able to produce accurate results for the one-dimensional conduction (through the plate) and two-dimensional conduction simulations (through the plate and axially along the plate). However, for most simulation application modes employed to model fuel plate conduction in conjunction with fluid flow, COMSOL returned cladding surface temperatures well below those expected based on legacy models. While the apparent heat transfer was in excess of expected values, COMSOL was able to return credible turbulent conductivity values for the fluid. One possible conclusion is that the legacy HFIR method is overly conservative in estimating heat transfer. The more likely conclusion however, is that the COMSOL solution is sensitive to mesh density and other model details that are in a preliminary stage at this point in the research.

(This page blank)

3. FUEL DEVELOPMENT

HFIR fuel plates possess unique characteristics that add complexity to the fuel fabrication process. The fuel concentration is varied in both the radial and axial directions (graded fuel). A boron carbide burnable poison is distributed with a graded concentration within the fuel plate. Furthermore, the fuel plates are formed radially to an involute profile. The varied concentration of fuel and burnable poison coupled with the involute shaped fuel plates introduces several challenges to the fabrication and inspection processes used in the production of HFIR fuel. Issues that are of considerable importance to HFIR fuel fabrication will be identified and these will form the basis of quality assurance requirements that will be part of a fuel specification for a manufacturer. Some machining tests have been conducted with foil surrogates, again, to aid in the development of an appropriate fuel specification for a manufacturer.

The studies reported here were conducted during the first quarter of FY08. Subsequent to that time, work at ORNL was suspended. Contour foil development at the Idaho National Laboratory proceeded during the remainder of FY08 but was based on an entirely different process than the studies presented here. (INL staff constructed a shaped ingot of U-10Mo, enclosed it in a steel casing, rolled the combined package to achieve HFIR fuel plate dimensions, and then separated and disposed of the steel casing.)

3.1 HFIR-Specific LEU Fuel Qualification Issues

To accommodate the graded fuel requirement, the monolithic LEU fuel design utilizes a fuel foil with varied thickness. One proposed thickness variation design is shown schematically in Fig. 3.1. There are number of potential issues that could arise during the development of fabrication and inspection methods and these are listed subsequently. This list, shown schematically in Fig. 3.2, is not intended to be all inclusive but only to illustrate issues that are being, or will likely need to be addressed as the LEU fuel development effort moves forward.

1. Clad thickness, tolerances, acceptance limits, and the measurement thereof.
2. Interlayer fracture or tearing that may occur during plate fabrication, plate forming, or in service. The example shown in the figure envisions interlayer tearing due to the stress concentration at a transition in foil thickness. This issue is likely intensified during plate forming.
3. Interlayer/diffusion barrier thickness, tolerances, acceptance limits, and the measurement thereof. The example, illustrated in Fig. 3.2, assumes interlayer thickness variations that arise during the co-rolling of the zirconium layer with the contoured fuel foil due to the different rolling behaviors of the U-Mo and Zr materials.
4. Void formation during plate fabrication and forming. A void formed at the edge of the fuel foil during the co-rolling of the fuel foil and interlayer is presented in the figure.
5. Foil, interlayer, and clad bonding. The definition and characterization of adequate bonding at the U-Mo/Zr/Al interfaces may be difficult to quantify.
6. Foil thickness tolerances, acceptance limits, and the measurement thereof.
7. The characteristics of the transitions in fuel foil thickness (corners). The minimum/maximum radius at transitions in foil thickness needs to be established to ensure adequate bonding and to mitigate stress concentrations.
8. Edge conditions of the fuel foil. The example presented in the figure assumes that the foil and interlayer are a co-rolled composite assembly that will need to be trimmed (blanked) to final size prior to clad bonding. This scenario leaves the U-Mo in contact with the Al cladding at the edge(s) of the fuel foil.

In addition to the above mentioned items, issues related to the presence of burnable poisons in HFIR fuel plates need investigation. The requirements of burnable poison concentration and form (elemental boron verses boron carbide or the use of alternative neutron absorbers) need to be studied so that methods for burnable poison inclusion in fuel plates can be better addressed. The impact of burnable poison inclusion on the overall fuel plate production process will also need to be evaluated.

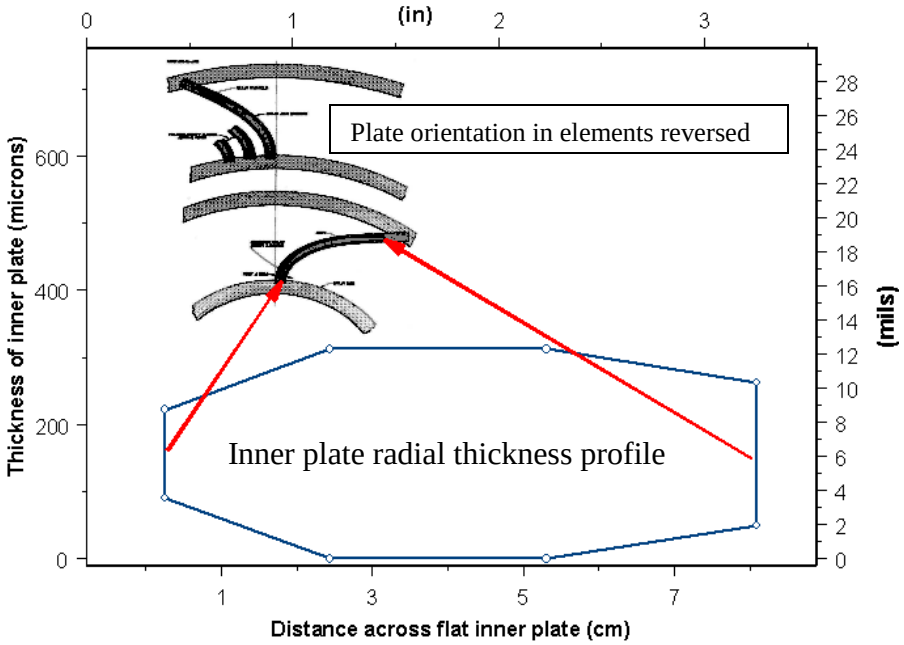

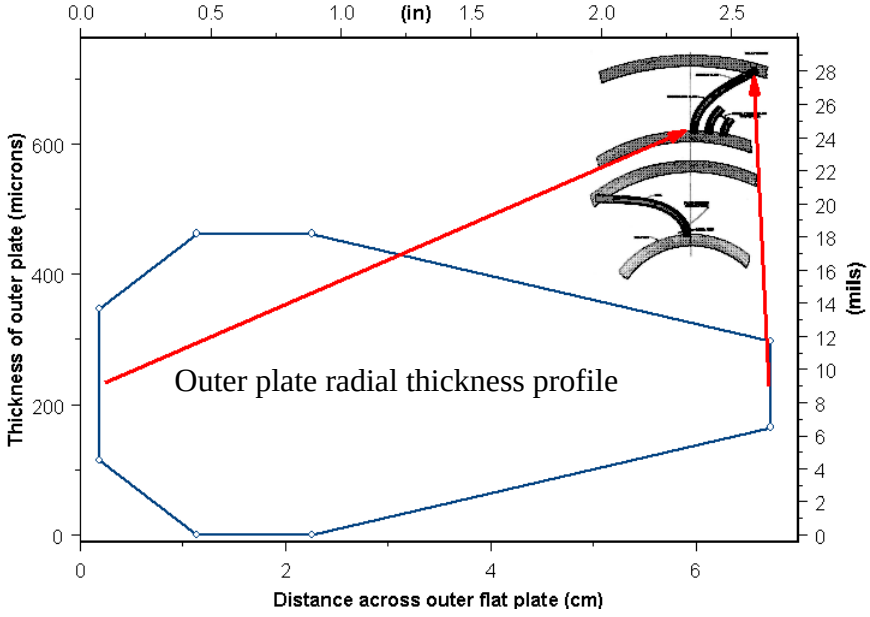

Fig. 3.1. A proposed HFIR fuel meat grading design.

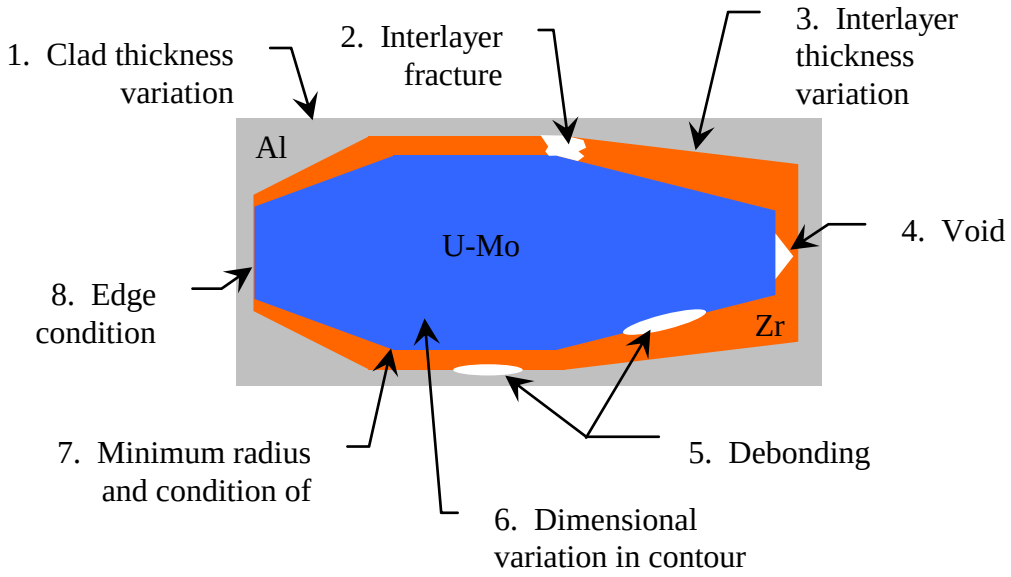

Fig. 3.2. Schematic representation of a radial cross section of a HFIR fuel plate with a contoured fuel foil illustrating several potential fabrication and inspection issues.

The generic fuel qualification plan under development at Idaho National Laboratory is not intended to and therefore does not address the issues of graded fuel foils, curved fuel plates, and the use of burnable poisons. These are key characteristics of HFIR fuel therefore; additional fuel development and reactor analysis will be needed to define the critical issues and to establish tolerances and acceptance limits for these issues.

3.2 Surrogate Fuel Foil Machining Study

As described in a previous study[1], experiments with flat (not contoured) steel foil samples 0.015 to 0.020 inch thick (representative of monolithic U-Mo fuel foils) were conducted with encouraging results. The steel foil samples in those experiments were held in place using a magnetic chuck and thickness variations on the order of 0.0002 inch were demonstrated.

In FY2008, contour grinding experiments were continued. Steel shim stock 0.020 inch thick was again employed as a surrogate for U-Mo. Samples two inches wide by eight inches long were cut from the procured steel shim stock by shearing and by electrical discharge machining (EDM). (EDM is a machining method that uses a continuous series of electrical discharges, or arcs, from an electrode to erode the work piece as the electrode passes through the material along a pre-programmed path.) A wire electrode EDM was used to cut foil grinding samples from the shim stock sheets. A comparison of the cut edge of sheared and EDM samples is shown in Fig. 3.3. The shearing process left a roll-over protrusion on the edge of the steel samples that had to be removed by filing prior use in contour grinding experiments. Due to the fact that EDM places no mechanical load on the work piece as it is cut, the edge of the EDM samples were square and did not require additional work prior to use as contour grinding samples. Note that the ramifications of the rolled edge from shearing on clad bonding or heat loads in service are unknown but merit consideration.

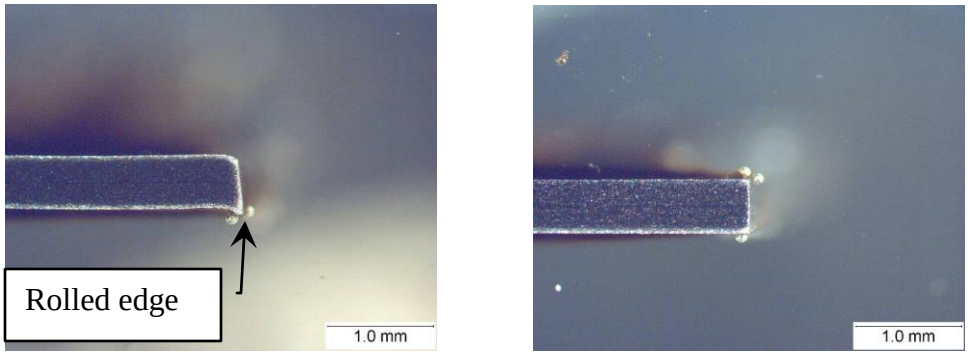

Sheared edge

Electro-discharge machined (EDM) edge

0.020 thick 1010 mild steel samples

Fig. 3.3. The characteristics of sheared and EDM foil edges.

3.2.1 Contour grinding with the vacuum chuck

For the initial contour grinding experiments, a custom designed vacuum chuck was fabricated to hold the steel foil samples during the grinding. A picture of the vacuum chuck showing the vacuum connection fitting and suction grooves is presented in Fig. 3.4. The Chevalier CNC surface grinder (shown in Fig. 3.5) was programmed to produce the 2-D contour shown schematically in Fig. 3.6. The initial grinding experiment using the mild steel shim stock held by the vacuum chuck was unsuccessful. Part way through the grinding sequence the work piece was dislodged from the vacuum chuck and ejected from the grinding table.

Inspection of the sample revealed bowing which caused the foil sample to "lift off" and break the seal with the vacuum chuck. It was initially believed that the sample bowing was due to residual stress in the shim stock blank from the production rolling process. Annealing the samples was considered but not performed. Likely a vacuum chuck could be designed that would provide better retention of the work piece (less leakage).

3.2.2 Contour grinding with the magnetic chuck

Additional grinding experiments were conducted using a magnetic chuck to determine if increased holding force could overcome the bowing tendency. Experiments using the magnetic chuck showed improvement, but were also unsuccessful. The samples tended to stay on the magnetic chuck longer, but they eventually became dislodged and were ejected. Further inspection revealed increasing amounts of bowing with increased grinding, and it was noticed that the edge of the foil samples was being plastically deformed and rolled over the edge of the magnetic chuck. A picture of a partially ground mild steel sample is shown in Fig. 3.7. An enlargement of the plastically deformed edge is also shown in the figure. The appearance of the rolled edge demonstrated that the bowing problem was not due to residual stresses as initially believed, but was instead due to plastic deformation imparted to the sample by the grinding process.

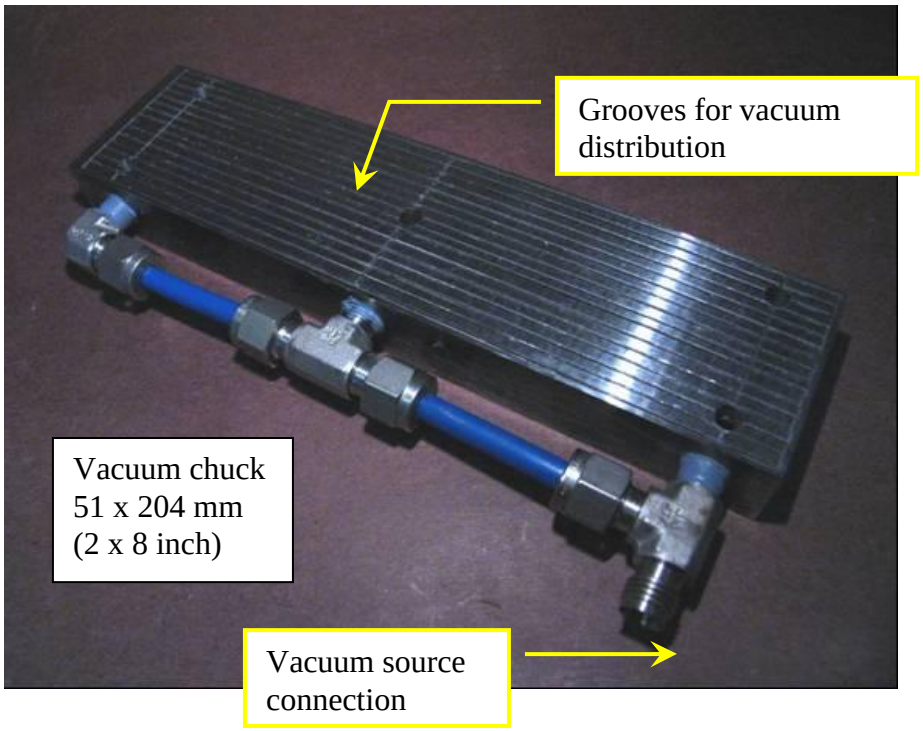

Fig. 3.4. The custom fabricated vacuum chuck used to hold 2 inch x 8 inch surrogate fuel foils for evaluation of contour grinding techniques.

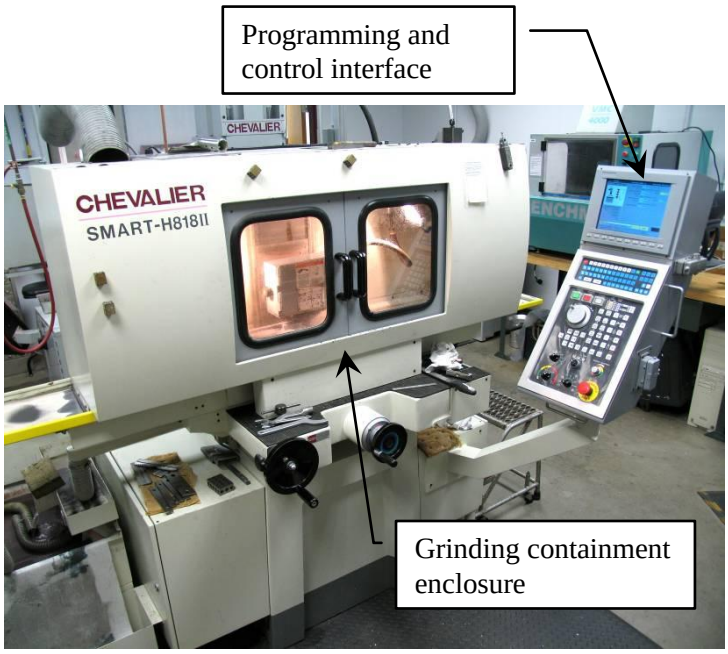

Fig. 3.5. The Chevalier CNC surface grinder used in the foil contour grinding study.

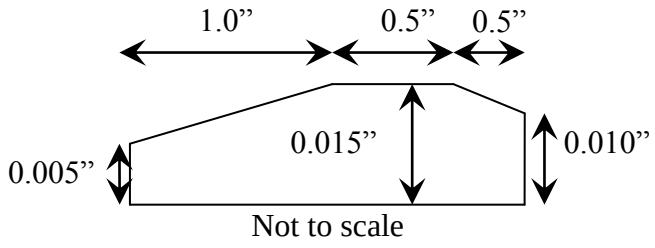

Fig. 3.6. Profile attempted in initial contour grinding experiments.

3.2.3 *Plastic deformation analysis*

An analysis of the potential for plastic deformation during grinding was conducted. The basis for the deformation analysis is shown schematically in Fig. 3.8. As the grinding wheel contacts the work piece, it applies a compressive load. The grinding wheel is rotating while the compressive load is applied thus causing material to be abrasively removed from the work piece.

The compressive load also causes a deflection of the work piece material, therefore as the grinding wheel traverses across the surface of the material, some material is removed ($\Delta_{removed}$) while some is deformed ($\Delta_{deformed}$) or pushed away by the grinding wheel. The deflection induced by the grinding wheel can be elastic (non-permanent or spring like) or a combination of elastic and plastic (permanent deformation left in the material). To prevent plastic deformation during grinding, the minimum down feed of the grinder ($\Delta_{down\ feed}$) needs to be less than the deflection that causes yielding in the sample ($\Delta_{down\ feed} < \Delta_{yield}$).

The amount of plastic deformation induced in the work piece is controlled by the compressive load applied by the grinding wheel. The magnitude of the compressive force is controlled by the down feed of the grinding wheel and the properties of the work piece. The potential for causing plastic deformation in the steel samples by grinding was estimated by comparing the minimum down feed of the grinding wheel to the deflection when the material reaches its yield point (Δ_{yield}). The deflection at the yield point was calculated based on the Hooke’s law and the modulus (E), yield strength (σ_{yield}), and thickness of the material.

The results of the analysis are shown in Table 3.1. The deflection at the yield point for the mild steel sample was 0.02×10^{-3} inch while the minimum down feed of the grinder was 0.10×10^{-3} inch, a factor of five greater. The same calculation was done for U-10Mo, and those results (also shown in Table 3.1) demonstrate that grinding may be a viable method for U-10Mo since the deflection at yield for U-10Mo is greater than the minimum down feed of the grinding machine.

3.2.4 Contour grinding of tempered steel surrogates

The yielding analysis was also used to find a more representative surrogate to use in continued grinding studies. Blue tempered steel shim stock was readily available, inexpensive and, while not the best match for U-Mo in terms of grinding properties, was much better than mild steel.

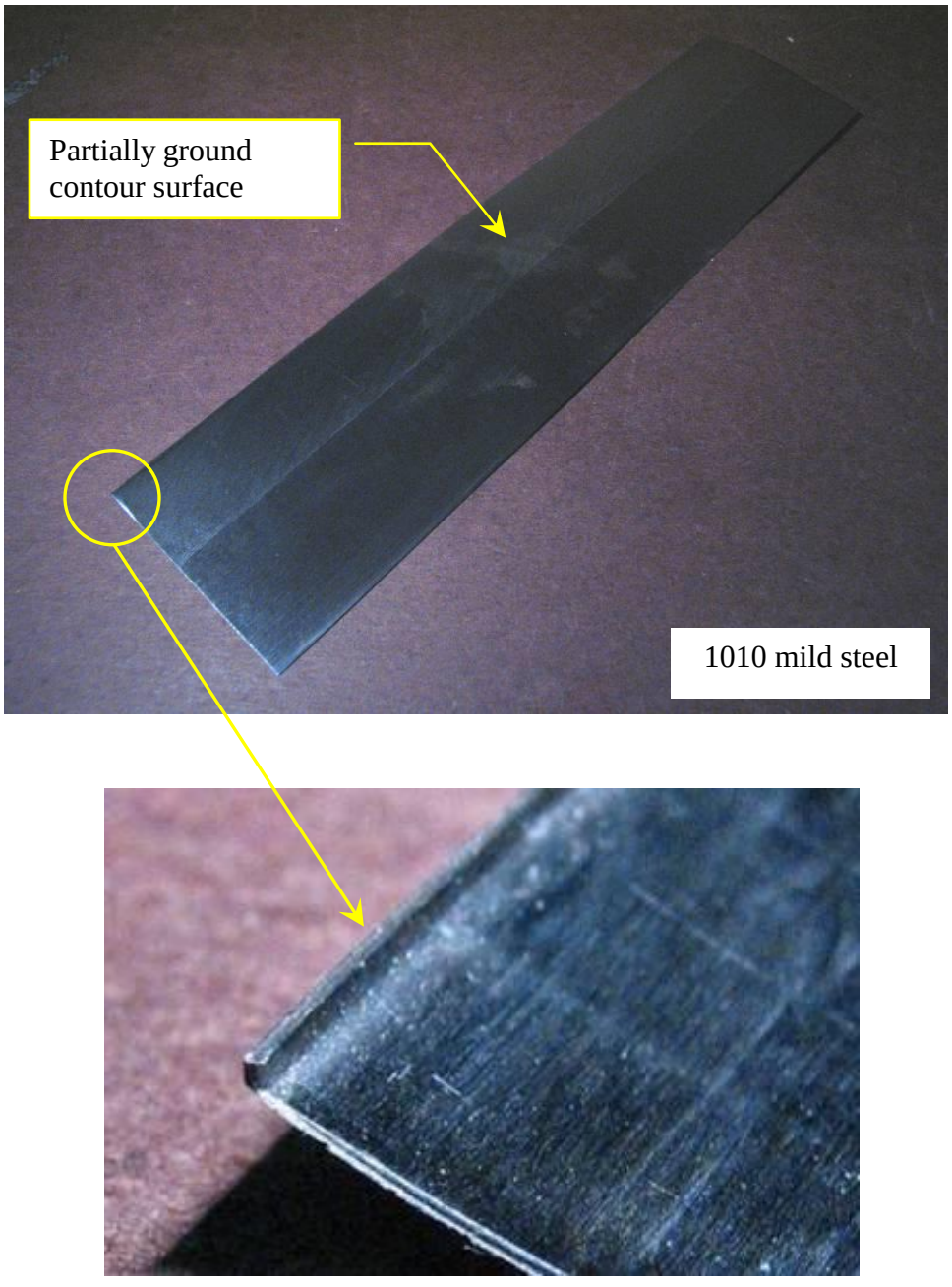

Starting material 2 x 8 x 0.020 inch thick shim stock

Fig. 7. Mild steel sample with partial contour ground surface.

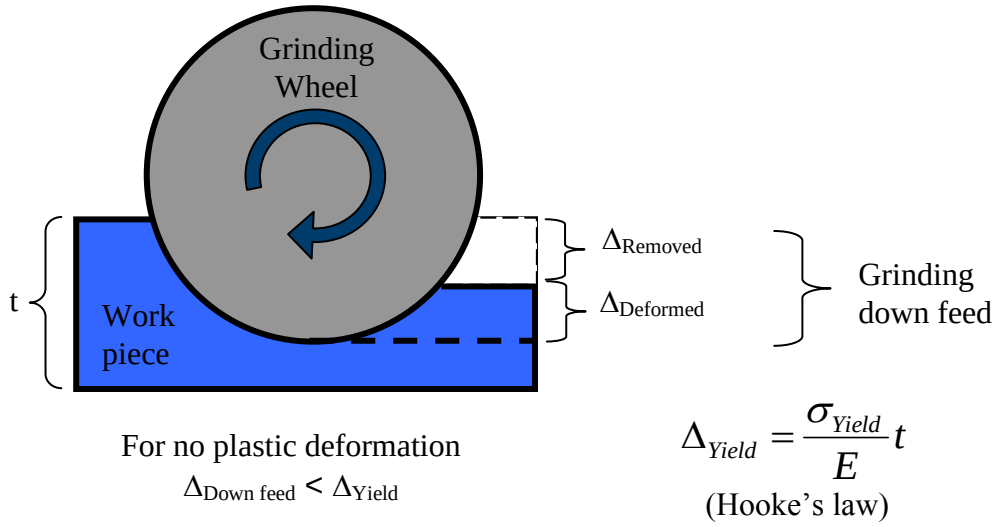

Fig. 3.8. A schematic explanation of the mechanism responsible for the plastic deformation induced in the surrogate fuel foil samples during contour grinding.

Contoured grinding experiments with blue tempered steel using the magnetic chuck were conducted with much improved results. Bowing and edge roll over were still present, but to a lesser extent. Pictures of the contour ground tempered steel sample are shown in Fig. 3.9, and Fig. 3.10 shows a comparison of the grinding induced edge roll-over of mild steel and tempered steel.

Table 3.1. Material properties and deflection limits necessary to avoid plastic deformation for surrogate and U-10Mo materials

	σ_{Yield} (ksi)	E (Msi)	Δ_{Yield} (10^{-3} in.) (Assuming t = 0.015in.)
1010 steel	30	30	0.02
Blue tempered steel	100	30	0.05
U-10Mo	130	12	0.16
Minimum grinding down feed			0.10

3.2.5 Contour production using EDM

The problems with plastic deformation encountered during grinding experiments indicated that wire-EDM, a cutting process that does not apply loads to the work piece, might be a feasible alternative. Two EDM contouring experiments were carried out. The first, shown in Fig. 3.11, was a combined grinding and EDM effort, and the second, shown in Fig. 3.12 was an all-EDM experiment. The combined grinding and EDM experiment involved grinding the contour of the fuel foil on a relatively thick piece of stock, and then cutting the foil thickness using EDM.

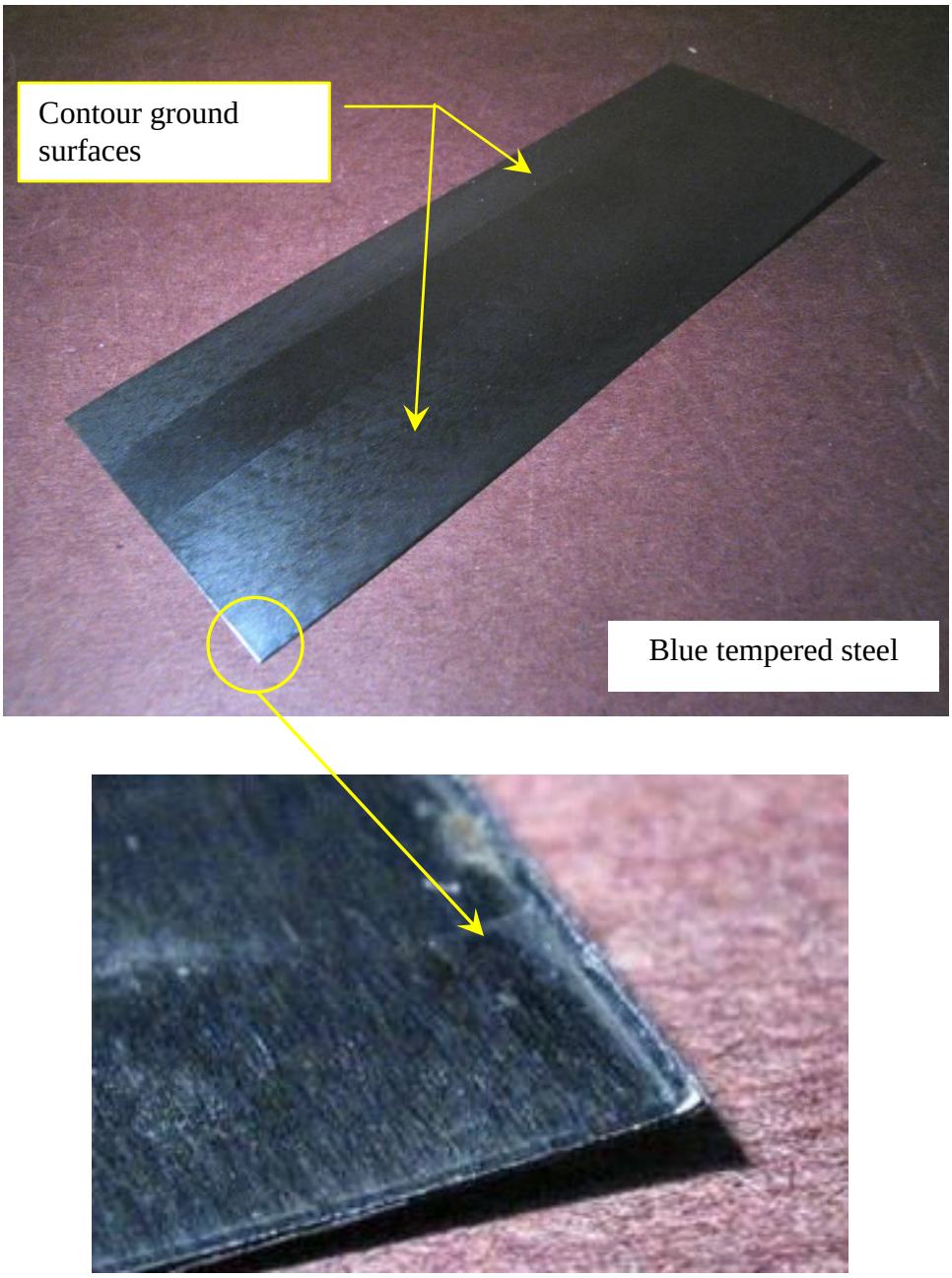

Starting material 2 x 8 x 0.020 inch thick shim stock

Fig. 3.9. Blue tempered steel contour ground sample.

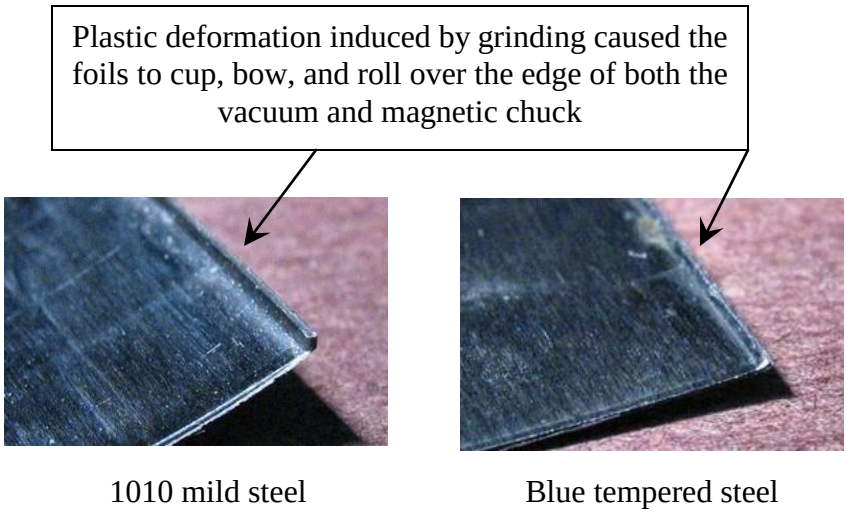

Fig. 3.10. The appearance of the rolled edge of the contour ground surrogate fuel foils.

The photograph in Fig. 3.11 shows the mild steel foil sample (a thick tempered sample was not procured) that was produced by the combined grinding EDM experiment. The uneven edge in the sample was caused by bowing of the foil as it was cut from the thick stock. The bowing was again due to grinding induced plastic deformation. Also shown in Fig. 3.11 is a schematic representation of the EDM wire (ride line) making the thickness cut (wire EDM cutting direction is indicated by the red arrows).

An all-EDM contouring experiment was also conducted using a mild steel bar stock. This experiment worked well. A picture of the foil sample produced completely by EDM is shown in Fig. 3.12 along with a schematic view of the EDM cutting process with the solid red line representing the EDM wire and the dashed red line representing the EDM cutting path.

The accuracy of the EDM contour cutting and the resulting surface finish was evaluated using a Taylor Hobson surface profilometer. The results are shown in Fig. 3.13 and Table 3.2. Figure 3.13 is a profile trace at one axial location on the contoured foil sample. The trace shows that the contour was accurately produced, but since it is a tracing of only one axial location, the variation along the length of the sample is not known and was not measured. The surface roughness data in Table 3.2 demonstrates that the EDM surface roughness is up to ten times larger than that produced by grinding. (The two roughness parameters measured were Ra, which is the arithmetic mean of the absolute departures of the roughness profile from the mean line, and Rz, which is the numerically average height difference between the five highest peaks and five lowest valleys.) It is possible that optimization of the EDM parameters could change the surface roughness, but that was not explored in this study. Also, the effect of surface roughness on interlayer and clad bonding has not been demonstrated, therefore it is not known whether increased surface roughness is either a positive or a negative.

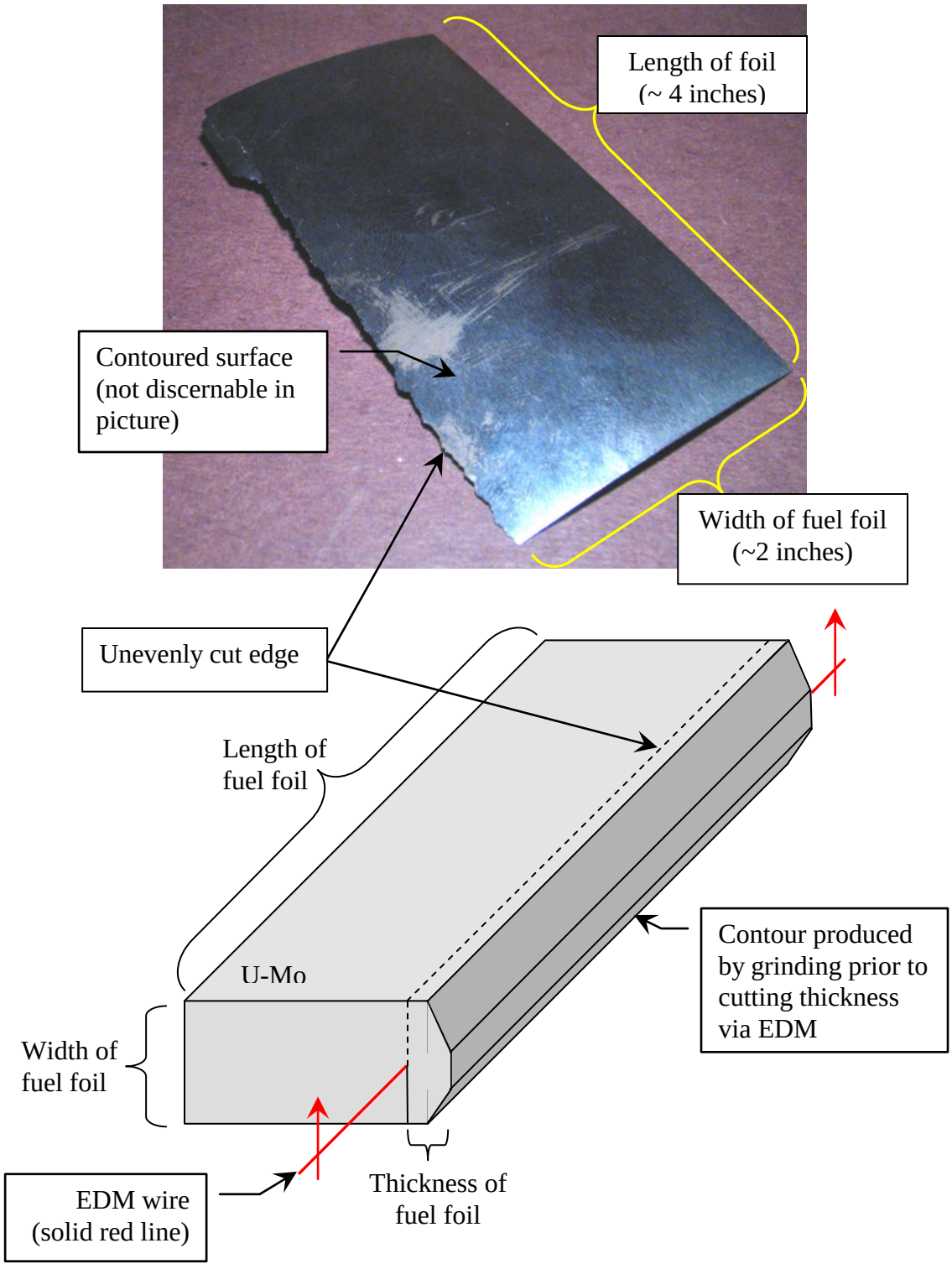

Fig. 3.11. Photographic and schematic views of the combined grinding and EDM surrogate fuel foil contouring experiment.

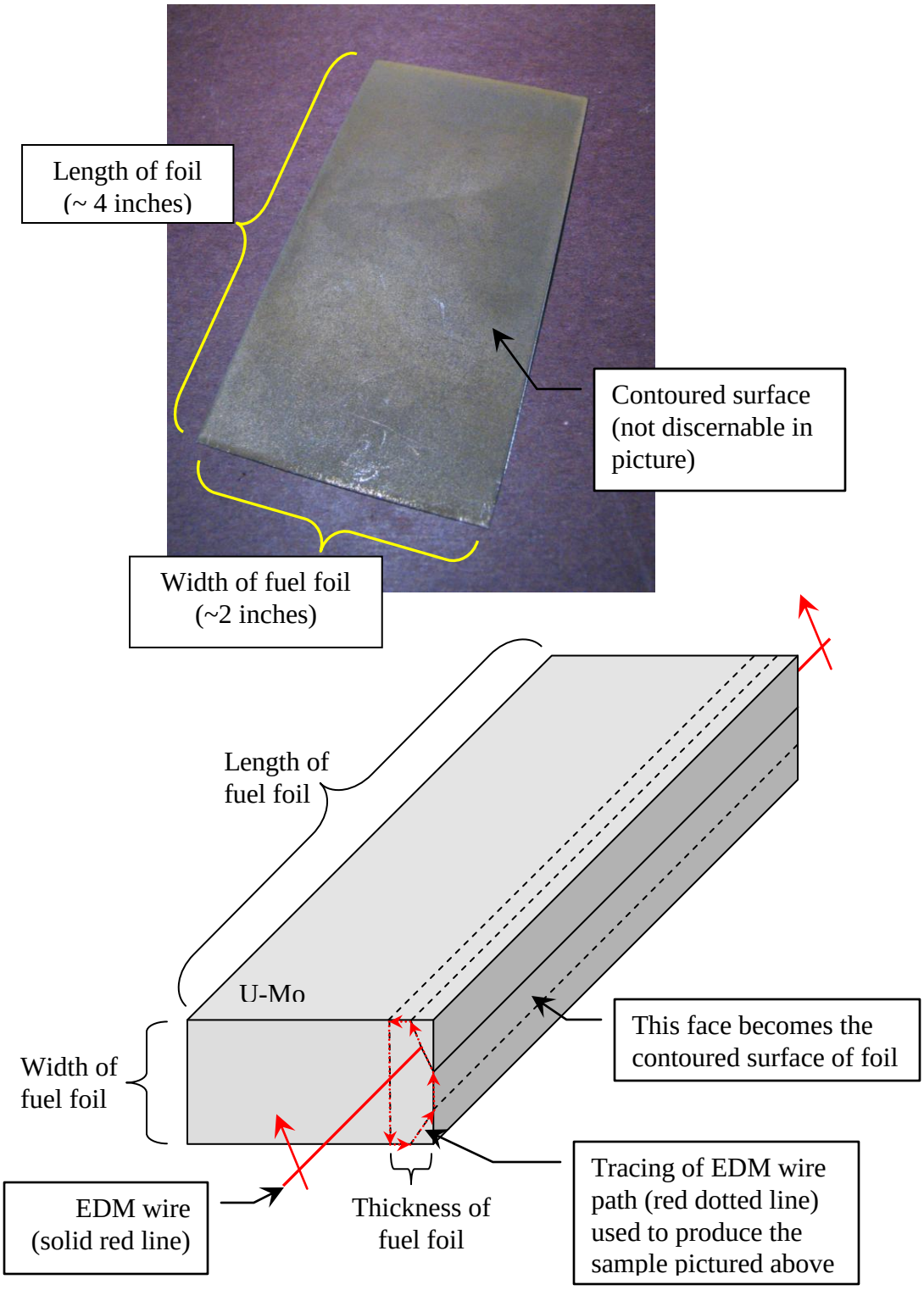

Fig. 3.12. Photographic and schematic views of the EDM surrogate fuel foil contouring experiment.

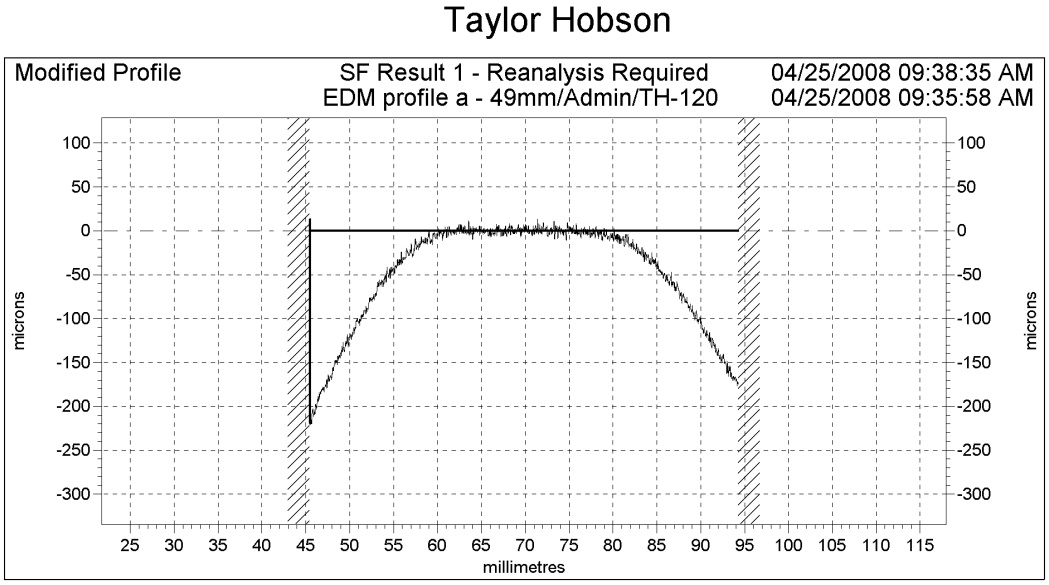

Fig. 3.13. Surface profile measurement of the EDM produced surrogate contoured fuel foil.

Note that both of the two EDM experiments used a relatively short (6 inches verses the 24 inch length of HFIR fuel plates) piece of stock material, and that the EDM cuts were made with the EDM wire parallel to the length direction of the fuel foil. Cutting in this geometry with full length fuel samples is not feasible, but these experiments were done this way because they required no special fixtures to hold the stock material in the proper orientation for cutting the contours.

Table 3.2. Surface finish measurements from the various contour grinding and EDM experiments

Wheel type	Ra (µm)	Rz (µm)
320grit flat	0.334	2.519
120grit flat	0.597	4.295
radius .25in/min	1.617	9.264
radius .125in/min	1.226	7.653
EDM	3.281	20.666
shim stock as recvd	0.830	4.800

3.2.6 Potential EDM method for contoured foil production

EDM appears to be a feasible method for producing contoured foils. The accuracy and repeatability need to be demonstrated along with the effect of surface finish on the interlayer and clad bonding processes. A method of recycling or safely disposing of the U-Mo particles present in the cutting fluid needs to be developed.

An EDM sequence that could produce the contoured foils is shown schematically in Fig. 3.14. The sketches in the figure show the EDM wire traversing through the U-Mo bar. The solid red line represents the EDM wire and the red arrows indicate the direction the wire is traversing as it makes a cut. The scenario for foil production is to make the contour cuts first (radial and axial) holding the U-Mo bar in the proper orientation with respect to the wire cut path, and then to cut the contoured foil from the bar in the last cutting step.

This scenario assumes that, the width and length of the U-Mo bar correspond to the width and the length of the fuel foil and that the thickness of each bar is sufficient to produce several foils and to provide a means for holding the bar in place during cutting. Recycle of the scrap is also assumed.

One potential disadvantage of EDM is the lack of speed. It is estimated that it would take on the order of a few hours for each cut to be made. In order for EDM to be production worthy, several machines would need to be running in parallel. This issue merits further investigation, but on first approximation it does not preclude EDM as a potential foil production method.

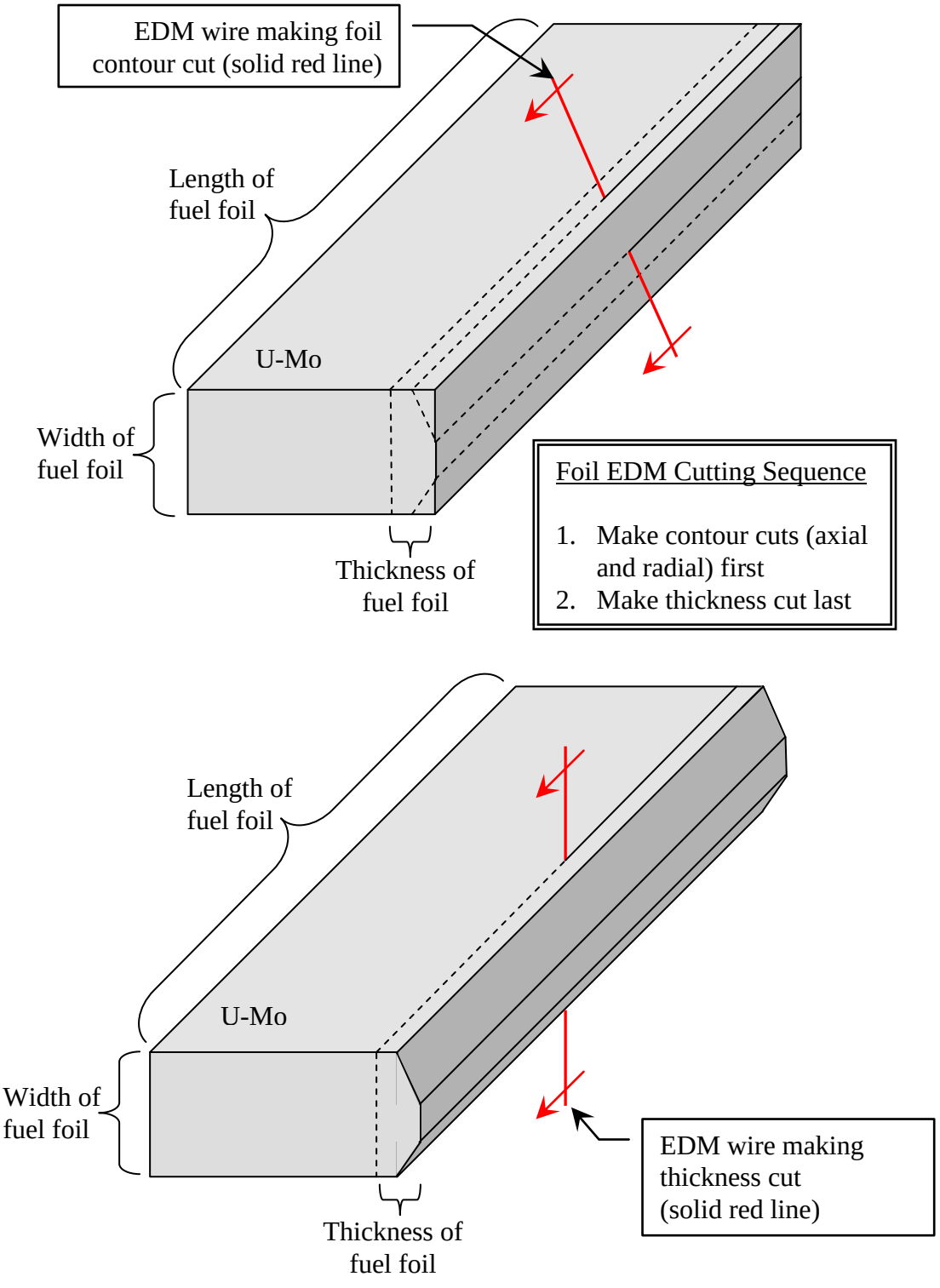

Fig. 3.14. Proposed EDM sequence for producing contoured fuel foils.

(This page blank)

4. STUDIES PLANNED FOR FY 2009

The proposed work in FY 2009 in the HFIR LEU conversion feasibility project will build upon and extend the results and scope of the studies presented in this document. The goals of the FY09 studies are to document a design currently believed to result in no degradation to the performance parameters for HFIR, translate this design to a manufacturing specification, continue to work to find a simplified and less costly LEU fuel design, and begin the transition from HEU to LEU by implementing a modified HEU, U_3O_8/Al fuel cycle. The reactor analysis effort is organized into six areas shown in Table 4.1.

ORNL support to fuel development activities is itemized in Table 4.2. As requested from program management, ORNL can supply support to irradiations being conducted by the RERTR program in the Advanced Test Reactor.

Table 4.1. ORNL reactor analysis activities proposed for FY 2009

Task area	Subtask	
	Title	Description
Reference U-10Mo fuel design (axial grading of foil)	Neutronics/thermal hydraulics design	Document neutronics and thermal hydraulics studies of reference LEU-10Mo design
	Process development	Develop and document engineering drawings and fuel specification for reference LEU fuel
	Computation model verification/validation	Compare ALEPH/MCNP to post-irradiation HEU measurements
Transition cycles (modify current HEU fuel to achieve LEU design burnup)	Neutronics	Determine U-235 loading and grading profile
	Process development	Determine changes to existing process to create higher-loaded HEU fuel plates
Improved U-10Mo fuel design (no axial grading)	Development of COMSOL based methodology	Multidimensional, steady state heat transfer model; turbulent mixing, incorporate diffusion barrier and nonbond assumptions in thermal-hydraulic model
	Thermal hydraulic committee	---
Preparation for regulatory review	Research publications for LEU validation; develop plan for LEU validation studies	---
Methods/model development	Cross section processing	Document 2-D SCALE model
	Deterministic methods implementation	Transport methods (ATTILA model); REBUS model
	Upgrade Monte Carlo Depletion methods	Migrate from ALEPH software to VESTA software
	Probabilistic combination of uncertainties (if funding is available)	Review/update TASHA code developed under Advanced Neutron Source Program
Program management	---	Report preparation
		Travel
		Meeting attendance

Table 4.2. ORNL fuels development activities proposed for FY 2009

Task name	Comment
Graded fuel development program	Perform tasks as identified by Idaho National Laboratory
Fuels program management	Includes support to review committees, meeting attendance, travel, and report preparation

5. REFERENCES

1. R. T. Primm III, R. J. Ellis, J. C. Gehin, G. Ilas, J. H. Miller, and J. D. Sease, *Design Study for a Low-Enriched Uranium Core for the High Flux Isotope Reactor, Annual Report for FY 2007*, ORNL/TM-2007/45, November 2007.
2. R. T. Primm III, R. J. Ellis, J. C. Gehin, K. T. Clarno, K. A. Williams, and D. L. Moses, *Design Study for a Low-Enriched Uranium Core for the High Flux Isotope Reactor, Annual Report for FY 2006*, ORNL/TM-2006/136, November 2006.
3. H. A. McLain, *HFIR Fuel Element Steady State Heat Transfer Analysis, Revised Version*, ORNL/TM-1904, Oak Ridge National Laboratory, Oak Ridge, Tennessee, December 1967 as appended by T. E. Cole, L. F. Parsly, and W. E. Thomas, Revisions to the HFIR Steady State Heat Transfer Analysis Code, ORNL/CF-85/68, April 7, 1986.
4. D.R.Vondy, T.B Fowler, and G.W. Cunningham III, *The BOLD VENTURE Computation System for Nuclear Reactor Core Analysis, Version III*, ORNL-5711, Oak Ridge National Laboratory.1981.
5. W. Haeck, *An Optimum Approach to Monte Carlo Burnup*, Ph.D. thesis, Ghent University, Belgium, 2007.
6. R. T. Primm III, *Reactor Physics Input to the Safety Analysis Report for the High Flux Isotope Reactor*, ORNL/TM-11956, March 1992.
7. X-5 Monte Carlo Team, *MCNP—A General Monte Carlo N-Particle Transport Code, Version 5*, LA-CP-03-0245, Los Alamos National Laboratory, April 24, 2003.
8. D. E. Peplow, *A Computational Model of the High Flux Isotope Reactor for the Calculation of Cold Source, Beam Tube, and Guide Hall Nuclear Parameters*, ORNL/TM-2004/237, November 2004.
9. N. Xoubi and R. T. Primm III, *Modeling of the High Flux Isotope Reactor Cycle 400*, ORNL/TM2004-251, August 2005.
10. N. Xoubi, *Characterization of Exposure-Dependent Eigenvalue Drift Using Monte Carlo Based Nuclear Fuel Management*, PhD dissertation, University of Cincinnati, 2005.
11. D. Chandler, R. T. Primm, III, and G. I. Maldonado, *Validating MCNP for LEU Fuel Design via Power Distribution Comparisons*, ORNL/TM-2008/126, November 2008.
12. R. D. Cheverton and T. M. Sims, *HFIR Core Nuclear Design*, ORNL-4621, Oak Ridge National Laboratory, 1971.
13. RSICC Computer Code Collection CCC-371, *ORIGEN 2.2*. Available from RSICC, Oak Ridge National Laboratory (2002).
14. N. Xoubi, and R.T. Primm III, *Investigation of Beryllium Internal Reflector Installation on the Fuel Cycle Length of the High Flux Isotope Reactor*, ORNL/TM-2004/252, Oak Ridge National Laboratory, August 2005.
15. *SCALE: A Modular Code System for Performing Standardized Computer Analyses for Licensing Evaluations*, version 5.1, vols. I–III, ORNL/TM-2005/39. Available from Radiation Safety Information Computational Center at Oak Ridge National Laboratory as CCC-732 (2005).
16. D.R.Vondy, T.B Fowler, and G.W. Cunningham III,, *Exposure Calculation Code Module for Reactor Core Analysis: BURNER*, ORNL-5180, Oak Ridge National Laboratory (February 1979).
17. C. Galvez Velit, R. T. Primm III, and J. C. Gehin, *Partial Safety Analysis for a Reduced Uranium Enrichment Core for the High Flux Isotope Reactor*, ORNL/TM-2007/226, April 2009.
18. L. Tschaepe, A.E. Ruggles, J.D. Freels, and R. T. Primm, III, *Evaluation of HFIR LEU Fuel Using the COMSOL Multiphysics Platform*, ORNL/TM-2008/188, March 2009.

19. R.T. Primm III, R.J. Ellis, J.C. Gehin, D.L. Moses, J.L. Binder, and N. Xoubi, *Assumptions and criteria for performing a feasibility study of the conversion of the High Flux Isotope Reactor core to use low-enriched uranium fuel*, CD Proceedings, PHYSOR 2006.
20. R.J. Ellis, J.C. Gehin, and R.T. Primm III, *Cross section generation and physics modeling in a feasibility study of the conversion of the High Flux Isotope Reactor core to use low-enriched uranium fuel*, CD Proceedings, PHYSOR 2006.
21. R.J. Ellis, J.C. Gehin, G. Ilas, and R.T. Primm III, *Neutronics feasibility study for conversion of the High Flux Isotope Reactor with LEU U-7Mo dispersion fuel*, ANS Transactions 96, 2007.

APPENDIX A

POWER DISTRIBUTION MEASUREMENTS FOR HFIR HEU FUEL

Benchmarking studies of diffusion/depletion methods for HEU HFIR fuel are documented in ref. 6. Corresponding studies with Monte Carlo methods (MCNP code[7]) had not been successfully performed until now due to the effort required to input spatially dependent tallies into the HFIR MCNP model[8, 9], the effort to modify the model to represent the reactor configuration at the time the measurements were conducted, and the inability to track a sufficient number of fission products (or, equivalently, the need to create a properly defined lumped fission product) for those Monte Carlo depletion methods previously available[10]. All three limitations are addressed (solved) by studies documented in ref. 11. A brief summary of results is presented subsequently.

A current 3-D MCNP model was modified to replicate the HFIR Critical Experiment 3 (HFIRCE-3) core of 1965. In this experiment, the power profile was determined by counting the gamma activity at selected locations in the core. "Foils" (chunks of fuel meat and clad) were punched out of the fuel elements in HFIRCE-3 following irradiation and experimental relative power densities were obtained by measuring the activity of these foils and comparing each foil's activity to the activity of a normalizing foil.

This analysis consisted of calculating corresponding activities by inserting volume tallies into the modified MCNP model to represent the punchings. The average fission density was calculated for each foil location and then normalized to the fission density of the reference foil. Power distributions were obtained for a clean core and a fully poisoned-moderator conditions. The observed deviations between the experimental and calculated values for both conditions were within the reported experimental uncertainties except for some of the foils located on the top and bottom edges of the fuel plates.

In order to validate MCNP via power density comparisons, a set of experimentally measured results are utilized. Tables A.1 and A.2 in Ref. 12 provide two data sets of relative power densities that were obtained during the HFIRCE-3 experiments. The core conditions corresponding to each of the two experiments are different and therefore provide two unique scenarios to model. The data in Table A.1 of Ref. 12 were obtained on September 9, 1965 for clean core conditions in which no boron was present in the moderator and the control rods were at a symmetrical position of 17.534 inches withdrawn from shutdown position. The set of data obtained on October 5, 1965, and listed in Table A.2 of Ref. 12, were measured under fully poisoned core conditions in which 1.35 grams of boron per liter of moderator was present and the control rods were fully withdrawn. Selected experimental data points from Ref. 12 tables are plotted in the following figures in this section along with the currently calculated values of local power densities.

The calculated eigenvalue (k_{eff}) under clean core conditions was 0.99561 ± 0.00013. Figure A.1 shows the radial relative power profile at the horizontal midplane. The impact of the axial water reflectors (water above and below the core) can be seen in Figs. A.2-A.3 (IFE = inner fuel element; OFE = outer fuel element). Accurate modeling of these power peaks is crucial to verify that LEU fuel is designed so that HFIR performance is not degraded by conversion of fuels.

The calculated eigenvalue (k_{eff}) under fully poisoned conditions (simulating end-of-life conditions) was 1.00593 ± 0.00013. Fig. A.4 shows the radial relative power profile at the horizontal midplane. The impact of the axial water reflector on the local power density is seen again in Figs. A.5-A.6.

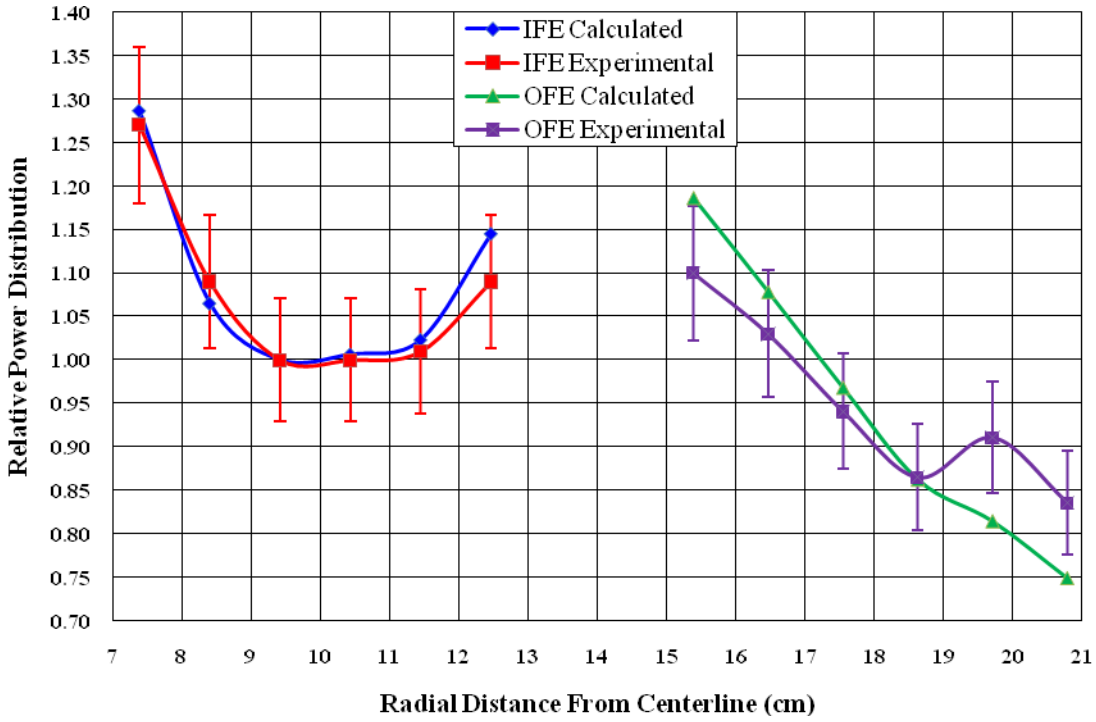

Fig. A.1. Radial relative power profile at horizontal midplane under clean core conditions

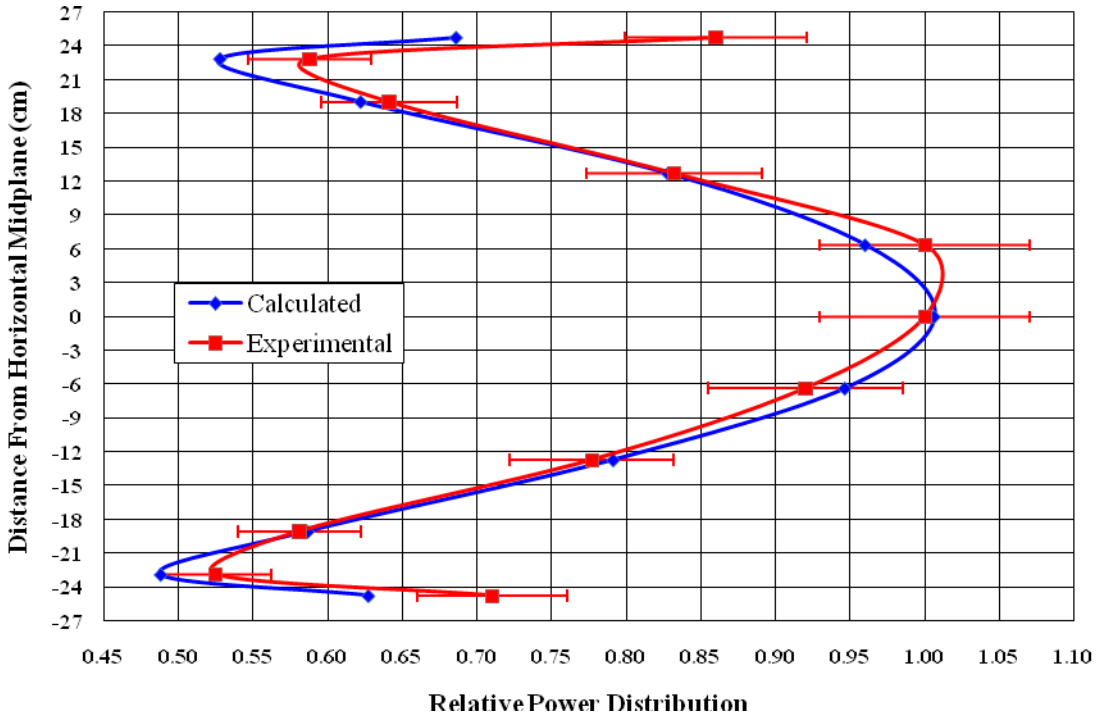

Fig. A.2. Axial relative power profile of foil 4 in IFE under clean core conditions.

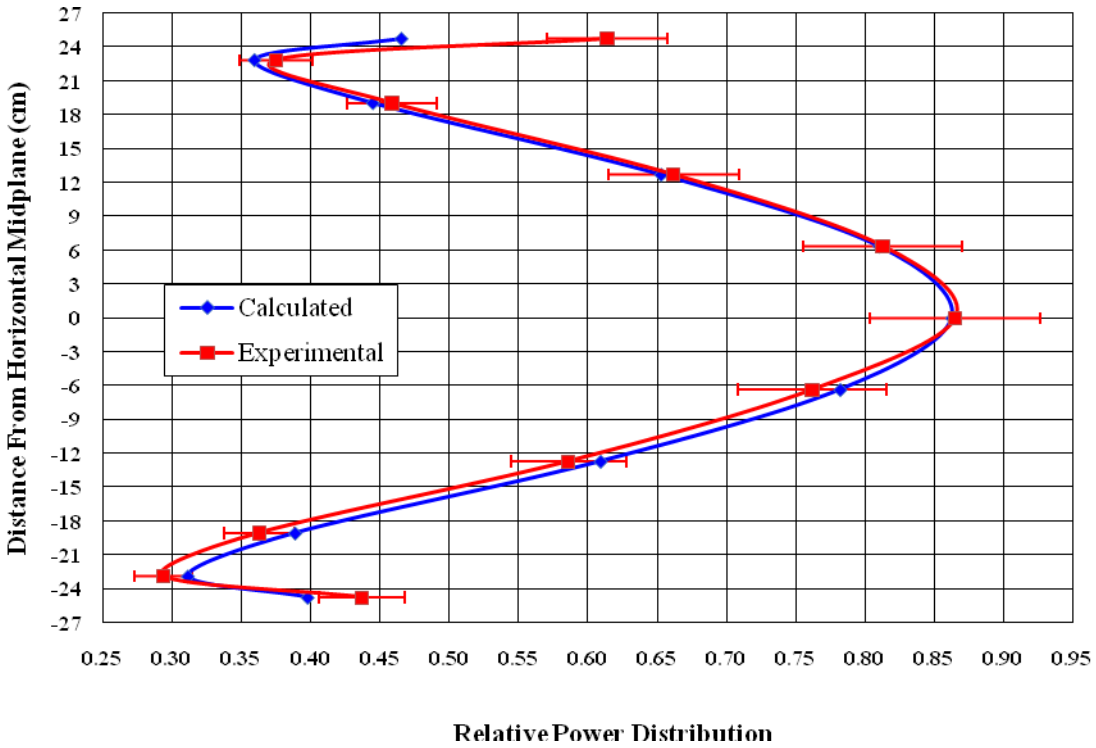

Fig. A.3. Axial relative power profile of foil 4 in OFE under clean core conditions.

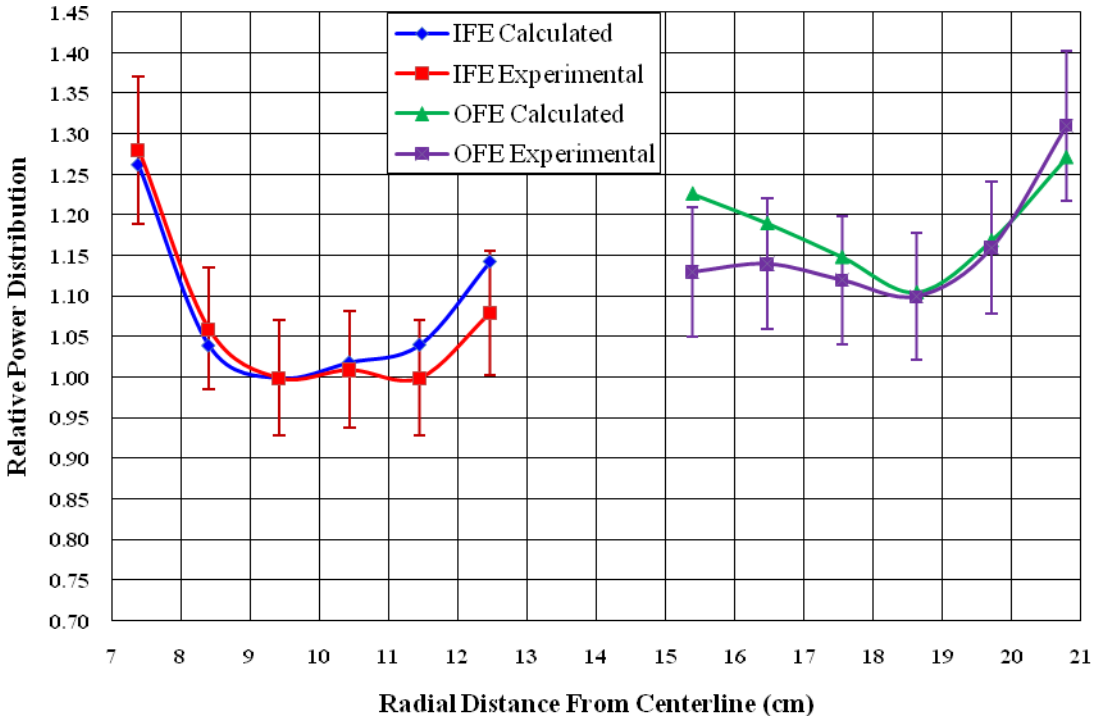

Fig. A.4. Radial relative power profile at horizontal midplane under fully poisoned core conditions.

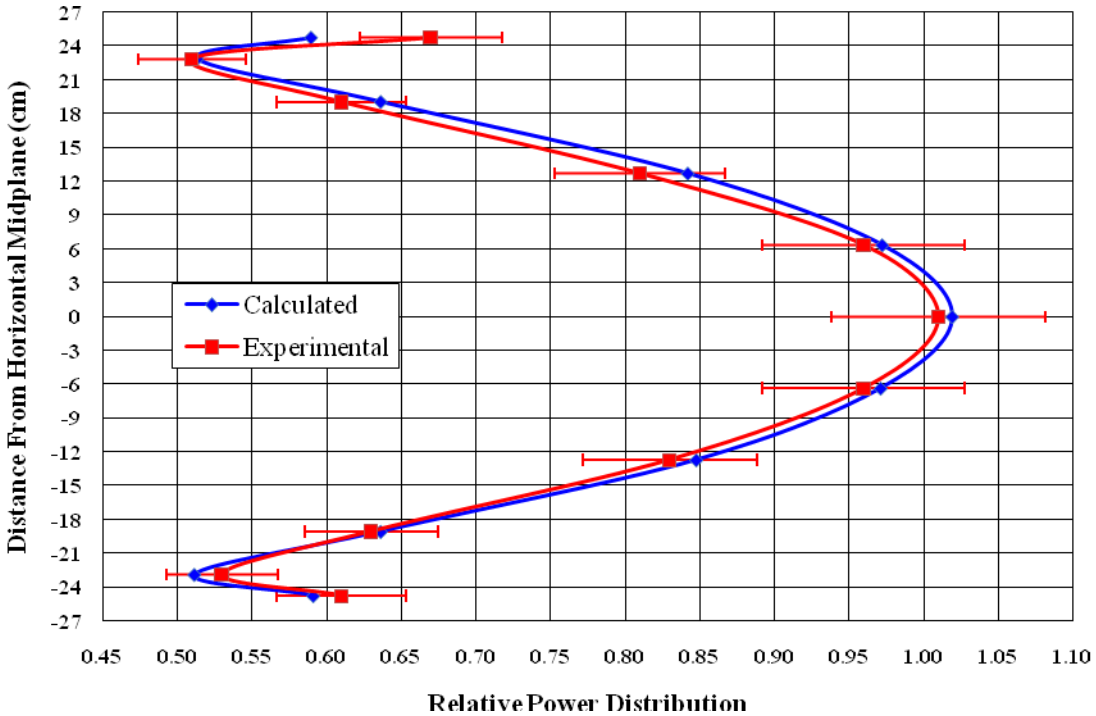

Fig. A.5. Axial relative power profile of foil 4 in IFE under fully poisoned core conditions.

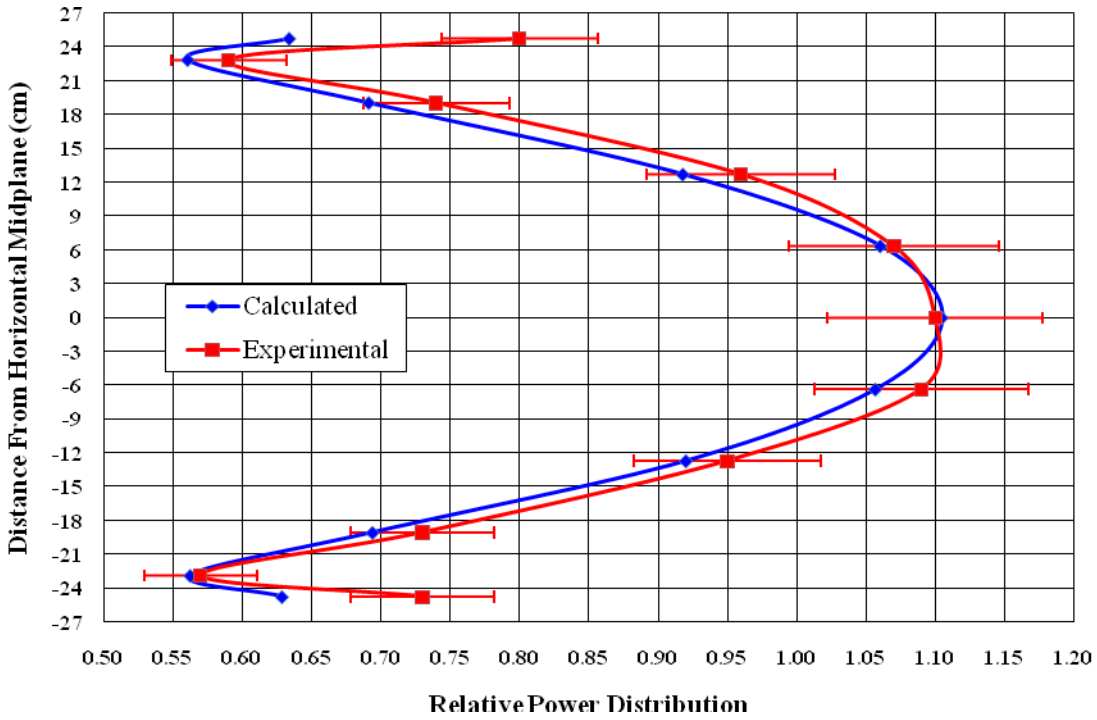

Fig. A.6. Axial relative power profile of foil 4 in OFE under fully poisoned core conditions.

(This page blank)

APPENDIX B

CYCLE LENGTH PREDICTION USING HFIR CYCLE 400 DATA

ALEPH[5] is a Monte Carlo-based depletion tool developed at SCK-CEN in Belgium. ALEPH couples a Monte Carlo transport code from the MCNP[7] family of codes (e.g., MCNP, MCNPX) and the point depletion and decay code ORIGEN 2.2[13]. It is a relatively user-friendly code; if an appropriate MCNP model of the configuration to be analyzed is available, the changes and/or additions to this model are minimal. At each depletion step, the transport flux solution from MCNP is used to generate the cross section data for the ORIGEN 2.2 depletion calculation; the isotopic composition data resulting from ORIGEN 2.2 is used in the subsequent MCNP transport calculation to obtain cross sections for the next depletion step, and so forth in an iterative manner. As compared to other Monte Carlo depletion tools, ALEPH has a particular approach in determining from MCNP the data needed for the ORIGEN 2.2 depletion calculation. Whereas other tools obtain the cross sections for depletion based on reaction rate tallies in the Monte Carlo transport calculation, ALEPH requires only flux tallies in a fine-group structure.

The one-group cross sections for ORIGEN 2.2 are obtained by weighting available pointwise cross section data with the MCNP-calculated fine-group flux. These pointwise cross section data are consistent with the cross section data used in the MCNP transport calculation, as both sets are pre-computed based on the same ENDF/B data files. The fine-group flux is tallied by MCNP in the energy range 10^{-5}eV to 20MeV using a 43000-group structure, with 5000 groups in the thermal region between 10^{-5}eV and 1eV, 36000 groups in the resonance region between 1eV and 1MeV, and 2000 groups in the fast region between 1MeV and 20MeV. Selected calculations, described subsequently, employ different boundaries for thermal, epithermal, and fast flux values.

B.1 ALEPH Model

Depletion simulations with ALEPH were performed for a revised HFIR cycle 400 core configuration. A correction applied to the reference[9] configuration used in previous studies consisted of changing the loading in the removable beryllium (RB) experiment locations. There are eight large RB experimental locations, designated in pairs, identified as RB-1A, RB-1B, RB-3A, RB-3B, RB-5A, RB-5B, RB-7A, and RB-7B. In the previous model, as illustrated in Fig. B.1a, five of the eight RB locations were occupied by dummy solid aluminum targets (powder blue color), one contained a europium liner (orchid color), and one a beryllium plug (golden rod color). In the corrected model, as illustrated in Fig. B.1b, there are four beryllium plugs, three dummy solid aluminum targets, and one europium target in the large RB locations.

As compared to the previous MCNP model, which had seven axial regions in each of the fuel elements, the MCNP model used with ALEPH contains 19 regions along the axial direction. As before, there are eight and nine regions along the radial direction in the inner fuel element (IFE) and outer fuel element (OFE), respectively. Geometry data for the radial and axial regions used in the ALEPH model are shown in Tables B.1 and B.2. The depletion simulation[5] was carried out using 24 depletion steps of 1-day length each, followed by one depletion step of 8 hours, for a total of 24.33 days of irradiation. The movement of the control elements during irradiation was included in the simulation.

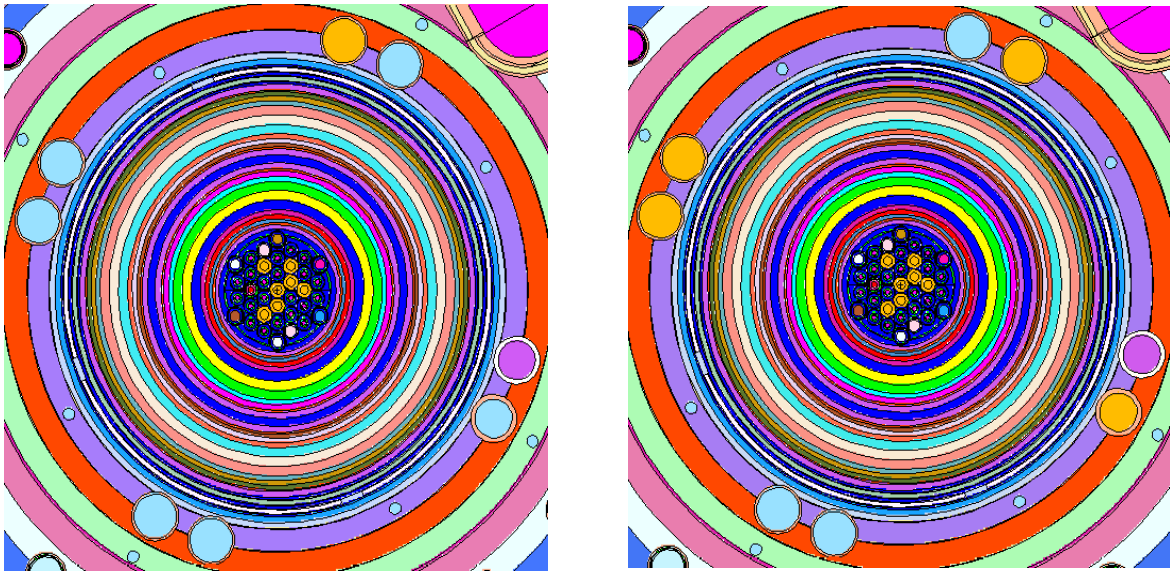

(a) previous model (b) corrected model

Fig. B.1. Changes in the RB locations for HFIR cycle 400 model.

Table B.1. Radial fuel regions in the ALEPH model for HFIR cycle 400

Inner fuel element		**Outer fuel element**	
region #	outer radius (cm)	region #	outer radius (cm)
1[a]	7.5	1	15.5
2	8.0	2	16.0
3	8.5	3	16.5
4	9.5	4	17.5
5	10.5	5	18.5
6	11.5	6	19.5
7	12.0	7	20.0
8	12.6	8	20.5
		9	20.978

[a] Inner radii are 7.14 cm and 15.12951 cm for IFE and OFE, respectively.

Table B.2. Axial fuel regions in the ALEPH model for HFIR cycle 400

Region #	Top edge [a] location (cm)	Thickness (cm)	Region #	Top edge [a] location (cm)	Thickness (cm)
1	25.4	0.4	11	-1.0	3.0
2	25.0	3.0	12	-4.0	3.0
3	22.0	3.0	13	-7.0	3.0
4	19.0	3.0	14	-10.0	3.0
5	16.0	3.0	15	-13.0	3.0
6	13.0	3.0	16	-16.0	3.0
7	10.0	3.0	17	-19.0	3.0
8	7.0	3.0	18	-22.0	3.0
9	4.0	3.0	19	-25.0	0.4
10	1.0	2.0			

[a] Location is with respect to the core midline at axial location 0.0 cm.

B.2 ALEPH Results

The variation, as obtained with ALEPH (MCNP-V), of the effective multiplication factor (k_{eff}) during the irradiation cycle 400 is illustrated in Fig. B.2. As seen, the value of k_{eff} at the end of cycle (EOC) is well predicted. While the beginning-of-life calculated k-effective value is higher than the "measured" value, neutron poisons initially present in the control/safety plates (^{182}Ta) and in the beryllium reflector (^{6}Li and ^{3}He) are not included in the MCNP model. Thus a calculated k_{eff} value higher than measured would be expected at beginning-of-life. As the cycle progresses, the control/safety plates are withdrawn from the core (impact of ignoring ^{182}Ta in the model is mitigated) and any strongly absorbing poisons present initially in the beryllium reflector are depleted. The excellent end-of-life agreement between calculated and measured k-effectives provides assurance that, collectively, reactivity reduction due to fission product poisoning and fissionable nuclide consumption is accurately estimated.

The ALEPH model includes detailed zoning on the radial and axial directions of the fuel elements regions that could be employed to extract time and spatial dependent power density data. The MCNP input files internally used by ALEPH to perform the transport calculation at each depletion step can be saved and used for tallying flux and reaction rates. The fission rate was tallied in each fuel region and used to calculate the spatial distribution of the relative fission density in the fuel elements; the data are shown in Tables B.3 and B.4 for beginning and end of cycle, respectively.

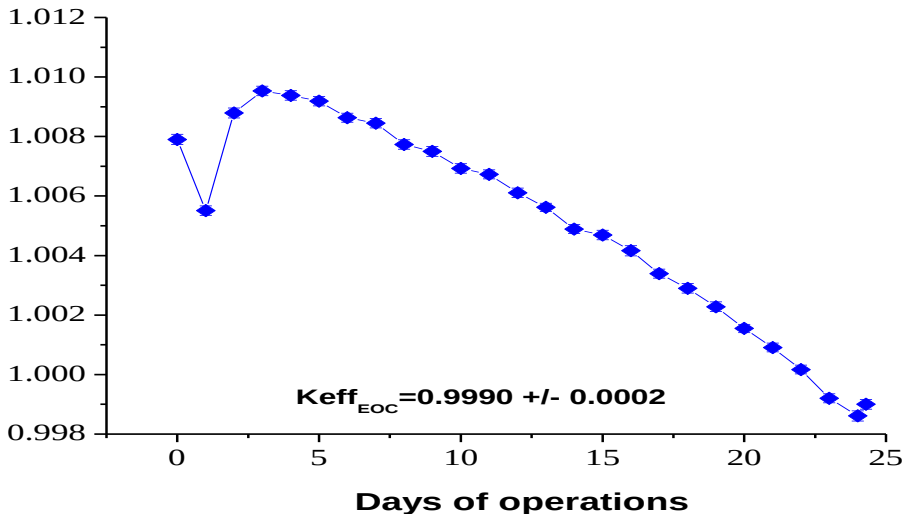

Fig. B.2. Variation of k_{eff} during irradiation for HFIR cycle 400.

The neutron flux at selected locations of interest – central target region, reflector, cold source edge – was tallied in three energy groups, with an energy structure as follow: thermal <0.625 eV; epithermal 0.625eV-100keV; fast 100keV-20MeV. As the flux tallies provided by MCNP are normalized to the source (i.e., 1 neutron), the values for the flux in n/cm^{2}s were obtained by multiplying the tally values by the total source. The total source was *S* was approximated as [14]

$$S = \frac{\nu P}{Ee} \qquad [1]$$

where ν is the average number of neutrons per fission (2.43 considered), *P* the reactor power in MW, *E* the average energy per fission in MeV (200.7 MeV/fission considered[14]), end *e* is a unit conversion constant. For 85 MW power, the total source is 6.42x10^{18} n/s. The flux results are shown in Table B.5. The nuclide inventory for actinides and important fission products – total mass in the core at EOC - is listed in Table B.6.

Table B.3. Relative fission density in IFE and OFE at BOC for HFIR cycle 400

Axial region #	IFE								OFE								
	r=1	r=2	r=3	r=4	r=5	r=6	r=7	r=8	r=1	r=2	r=3	r=4	r=5	r=6	r=7	r=8	r=9
1	1.050	1.050	1.087	1.147	1.220	1.281	1.222	1.144	1.155	1.155	1.174	1.196	1.176	1.019	0.781	0.596	0.467
2	0.885	0.885	0.844	0.819	0.810	0.813	0.812	0.816	0.914	0.914	0.852	0.803	0.736	0.626	0.510	0.414	0.352
3	0.924	0.924	0.871	0.829	0.807	0.808	0.820	0.842	0.937	0.937	0.878	0.826	0.755	0.645	0.531	0.439	0.376
4	1.056	1.056	1.004	0.961	0.940	0.948	0.959	0.985	1.092	1.092	1.028	0.975	0.902	0.781	0.654	0.554	0.481
5	1.205	1.205	1.141	1.097	1.075	1.081	1.098	1.122	1.247	1.247	1.181	1.129	1.047	0.923	0.806	0.711	0.650
6	1.342	1.342	1.267	1.211	1.190	1.203	1.219	1.252	1.387	1.387	1.316	1.256	1.179	1.054	0.941	0.858	0.806
7	1.436	1.436	1.362	1.306	1.277	1.289	1.314	1.350	1.498	1.498	1.426	1.371	1.287	1.157	1.043	0.963	0.911
8	1.489	1.489	1.417	1.365	1.337	1.361	1.389	1.421	1.584	1.584	1.508	1.446	1.362	1.233	1.125	1.047	1.003
9	1.524	1.524	1.451	1.391	1.372	1.392	1.423	1.455	1.637	1.637	1.560	1.495	1.412	1.286	1.193	1.130	1.099
10	1.524	1.524	1.457	1.398	1.378	1.396	1.427	1.468	1.642	1.642	1.564	1.504	1.423	1.298	1.207	1.163	1.141
11	1.517	1.517	1.441	1.389	1.368	1.385	1.411	1.454	1.621	1.621	1.548	1.481	1.395	1.270	1.173	1.107	1.068
12	1.481	1.481	1.404	1.349	1.323	1.336	1.361	1.402	1.555	1.555	1.477	1.414	1.330	1.200	1.084	0.998	0.940
13	1.409	1.409	1.335	1.281	1.253	1.267	1.284	1.317	1.456	1.456	1.383	1.324	1.240	1.111	0.993	0.909	0.852
14	1.291	1.291	1.225	1.174	1.152	1.165	1.179	1.203	1.335	1.335	1.267	1.208	1.129	1.000	0.889	0.804	0.748
15	1.159	1.159	1.098	1.054	1.031	1.038	1.055	1.076	1.193	1.193	1.124	1.071	0.992	0.866	0.740	0.642	0.579
16	1.024	1.024	0.968	0.923	0.896	0.905	0.914	0.930	1.027	1.027	0.968	0.916	0.840	0.712	0.572	0.458	0.379
17	0.892	0.892	0.836	0.796	0.768	0.765	0.772	0.791	0.877	0.877	0.821	0.769	0.695	0.579	0.456	0.356	0.289
18	0.849	0.849	0.808	0.777	0.763	0.761	0.757	0.765	0.843	0.843	0.784	0.733	0.666	0.553	0.429	0.332	0.264
19	1.002	1.002	1.037	1.091	1.152	1.197	1.147	1.073	1.059	1.059	1.073	1.083	1.057	0.885	0.652	0.469	0.351

Table B.4. Relative fission density in IFE and OFE at EOC for HFIR cycle 400

Axial	IFE								OFE								
region #	r=1	r=2	r=3	r=4	r=5	r=6	r=7	r=8	r=1	r=2	r=3	r=4	r=5	r=6	r=7	r=8	r=9
1	0.653	0.653	0.779	0.895	1.023	1.108	1.090	1.009	0.993	0.993	1.094	1.171	1.234	1.162	1.026	0.892	0.795
2	0.639	0.639	0.737	0.804	0.847	0.859	0.840	0.823	0.841	0.841	0.847	0.842	0.816	0.765	0.730	0.706	0.689
3	0.649	0.649	0.752	0.817	0.852	0.849	0.835	0.828	0.846	0.846	0.853	0.845	0.815	0.765	0.752	0.751	0.746
4	0.675	0.675	0.803	0.894	0.954	0.965	0.953	0.933	0.925	0.925	0.954	0.958	0.936	0.888	0.869	0.854	0.837
5	0.688	0.688	0.841	0.963	1.053	1.079	1.062	1.028	1.011	1.011	1.054	1.067	1.049	0.996	0.971	0.940	0.904
6	0.689	0.689	0.866	1.012	1.132	1.175	1.150	1.105	1.075	1.075	1.139	1.164	1.148	1.089	1.051	1.004	0.947
7	0.679	0.679	0.870	1.041	1.184	1.237	1.215	1.160	1.115	1.115	1.193	1.227	1.216	1.155	1.111	1.044	0.968
8	0.668	0.668	0.868	1.052	1.213	1.283	1.256	1.196	1.142	1.142	1.232	1.269	1.265	1.201	1.148	1.069	0.976
9	0.667	0.667	0.872	1.065	1.231	1.311	1.284	1.214	1.154	1.154	1.250	1.297	1.293	1.228	1.173	1.086	0.982
10	0.665	0.665	0.870	1.062	1.236	1.314	1.284	1.222	1.159	1.159	1.252	1.301	1.297	1.231	1.178	1.089	0.986
11	0.667	0.667	0.871	1.063	1.236	1.311	1.282	1.217	1.154	1.154	1.250	1.292	1.287	1.225	1.171	1.085	0.982
12	0.675	0.675	0.875	1.056	1.217	1.286	1.256	1.197	1.136	1.136	1.225	1.271	1.262	1.199	1.149	1.072	0.979
13	0.681	0.681	0.872	1.041	1.184	1.243	1.215	1.160	1.108	1.108	1.186	1.225	1.215	1.154	1.109	1.047	0.967
14	0.683	0.683	0.861	1.008	1.125	1.171	1.147	1.105	1.066	1.066	1.131	1.155	1.140	1.082	1.048	1.004	0.950
15	0.685	0.685	0.837	0.959	1.050	1.076	1.057	1.025	1.010	1.010	1.059	1.072	1.049	0.993	0.969	0.942	0.907
16	0.677	0.677	0.804	0.895	0.954	0.965	0.950	0.931	0.929	0.929	0.957	0.960	0.935	0.886	0.868	0.854	0.836
17	0.654	0.654	0.755	0.819	0.852	0.851	0.838	0.829	0.839	0.839	0.849	0.840	0.810	0.764	0.754	0.753	0.747
18	0.646	0.646	0.743	0.804	0.847	0.855	0.839	0.823	0.839	0.839	0.845	0.836	0.810	0.755	0.719	0.693	0.677
19	0.655	0.655	0.776	0.890	1.017	1.106	1.092	1.014	0.986	0.986	1.078	1.166	1.215	1.139	0.991	0.847	0.754

Table B.5. Neutron flux at BOC and EOC for HFIR cycle 400

Location	Time	Thermal flux (n/cm^2s)	Epithermal flux (n/cm^2s)	Fast flux (n/cm^2s)
Central target	BOC	2.2×10^{15}	1.3×10^{15}	1.1×10^{15}
	EOC	2.3×10^{15}	1.1×10^{15}	9.9×10^{14}
Cold source edge	BOC	6.8×10^{14}	2.4×10^{14}	9.0×10^{13}
	EOC	8.3×10^{14}	2.4×10^{14}	8.9×10^{13}
Reflector r=27 cm	BOC	6.0×10^{14}	6.5×10^{14}	4.1×10^{14}
	EOC	8.1×10^{14}	6.5×10^{14}	4.0×10^{14}

Table B.6. Nuclide inventory at EOC for HFIR cycle 400

Nuclide	**Mass (g)**	**Nuclide**	**Mass (g)**
B-10	0.203	Pm-147	11.960
B-11	12.480	Pm-148	0.257
Kr-86	15.840	Pm-148m	0.088
Zr-93	53.480	Pm-149	2.059
Mo-97	51.440	Sm-149	0.382
Tc-99	43.580	Sm-150	13.200
Ru-101	46.950	Sm-151	1.133
Ru-103	24.280	Sm-152	7.005
Rh-103	5.121	Sm-153	0.646
Rh-105	0.530	U-234	88.040
I-135	1.263	U-235	6785.000
Xe-131	18.640	U-236	502.300
Xe-133	23.270	U-238	532.000
Xe-135	0.054	Np-237	6.188
Cs-133	50.180	Np-238	0.134
Cs-134	1.531	Np-239	2.777
Cs-135	2.910	Pu-238	0.273
Ce-141	58.760	Pu-239	11.410
Pr-143	40.940	Pu-240	1.429
Nd-143	26.340	Pu-241	0.612
Nd-145	49.380	Pu-242	0.049
Nd-147	14.060		

(This page blank)

APPENDIX C

ALEPH/MCNP MODEL FOR HFIR LEU CORE

The MCNP model used for the HFIR LEU configuration is based on the 3-D MCNP model for HFIR HEU cycle 400[9] with the correction described in Appendix B of this report and similar to the HFIR LEU model used in previous studies. The HFIR cycle 400 model was developed to include six regions:

1. Flux trap target region (FTT)
2. Inner fuel element region (IFE)
3. Outer fuel element region (OFE)
4. Control element region (CR)
5. Removable reflector region (RB)
6. Beryllium permanent reflector region (PB)

As compared to the FTT model for revised cycle 400, where the 31 sites in the interior of the basket out of the 37 experimental locations in FTT included 28 dummy aluminum targets, one hydraulic tube, and two stainless steel targets, there are one hydraulic tube and 30 curium targets in the interior of the basket, as illustrated in Fig. C.1. The composition of the curium targets is listed in Table C.1.

Table C.1. Composition of curium targets in the HFIR LEU core model

Nuclide ID	Number Density (At/b-cm)	Nuclide ID	Number density (At/b-cm)
O-16	6.6358E-03	Am-243	3.7252E-05
Al-27	4.1858E-02	Cm-242	1.1234E-09
Pu-238	1.4608E-08	Cm-243	3.7128E-07
Pu-239	1.9706E-08	Cm-244	6.1759E-04
Pu-240	3.7969E-05	Cm-245	9.2061E-06
Pu-242	1.1256E-09	Cm-246	1.3000E-03
Pu-242	2.9825E-07	Cm-247	3.7719E-05
Am-241	1.5978E-04	Cm-248	2.5183E-04
Am-242	4.2253E-07		

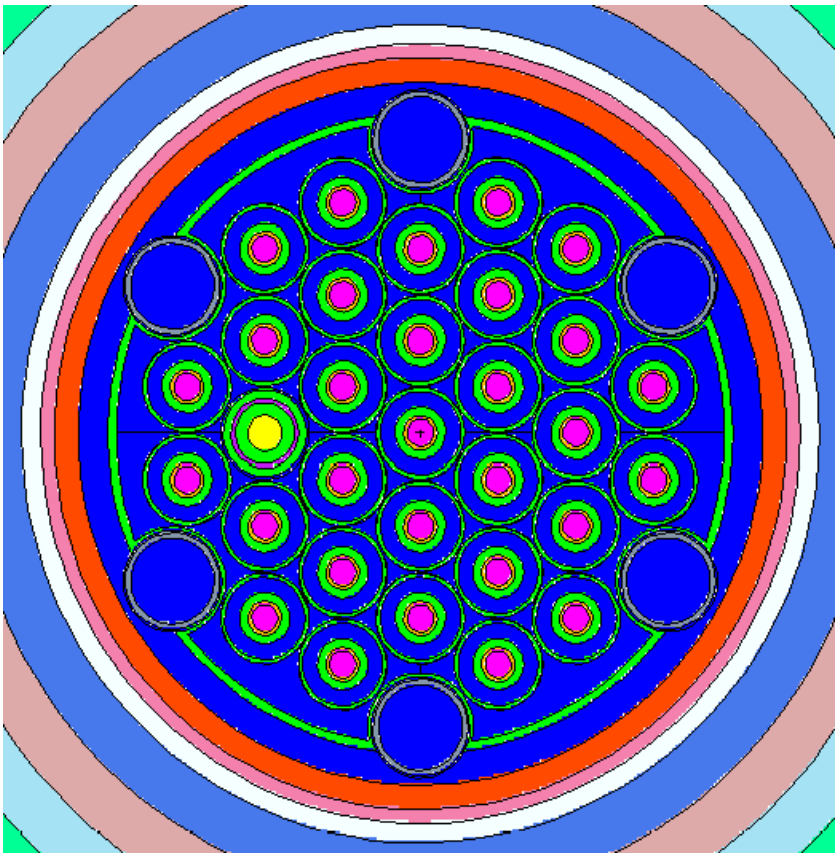

Fig. C.1. Flux trap region in the LEU core model (horizontal view).

The LEU fuel used in this study, previously selected as a reference fuel, consists of a monolithic uranium-molybdenum alloy, U-10Mo, which contains 90 wt% uranium and 10 wt% natural molybdenum. The uranium enrichment is 19.75 wt% ^{235}U. As used in the MCNP model for cycle 400, the fuel in the IFE region is modeled by homogenizing the fuel meat and aluminum cladding of the fuel plates and the water in between the fuel plates. The fuel in the IFE region is modeled as including eight radial regions with different ^{235}U concentrations to approximate the variation of the ^{235}U concentration in the radial direction of the fuel plate (i.e. radial fuel grading). The fuel region in the OFE is represented similarly to the IFE region, but with nine radial regions. The dimensions of the radial fuel regions in the IFE and OFE models are shown in Table C.2. Axially, the fuel element region was divided into 19 axial layers for calculation purposes; axial grading was used in some of the studied cases. The dimensions for the axial layers are shown in Table C.3. The selection of the axial layers dimension was done by studying the variation of the microscopic thermal fission cross section of ^{235}U as a function of the axial location, at it will be further discussed. All the other regions outside the fuel elements were represented as in the model for cycle 400. The location used for the control elements in the CR region varied in the studied LEU cases. Radial and axial cross sections of the model are illustrated in Figs. C.2 and C.3, respectively.

Table C.2. Radial fuel regions in the MCNP model for HFIR LEU

Inner fuel element		Outer fuel element	
region #	outer radius (cm)	Region #	outer radius (cm)
1[a]	7.50	1	15.16
2	8.50	2	15.50
3	9.50	3	16.50
4	10.50	4	17.50
5	11.50	5	18.50
6	12.50	6	19.50
7	12.59	7	20.50
8	12.60	8	20.99
		9	21.00

[a] Inner radii are 7.14 cm and 15.15 cm for IFE and OFE, respectively.

Table C.3. Axial fuel regions in the MCNP model for HFIR LEU

Region #	Top edge [a] location (cm)	Thickness (cm)	Region #	Top edge [a] location (cm)	Thickness (cm)
1	25.4	0.5	11	-1	8.4
2	24.9	0.5	12	-4.2	4.2
3	24.4	1.0	13	-12.6	4.2
4	23.4	1.0	14	-16.8	1.4
5	22.4	1.0	15	-21.0	1.0
6	21.0	1.4	16	-22.4	1.0
7	16.8	4.2	17	-23.4	1.0
8	12.6	4.2	18	-24.4	0.5
9	4.2	8.4	19	-24.9	0.5
10	1.0	2.0			

[a] Location is with respect to the core midline at axial location 0.0 cm.

C.1 Optimization of the Monte Carlo Model in ALEPH

A simplified 3-D MCNP model of HFIR was used for studying the trends in the thermal neutron flux and microscopic thermal fission cross section of ^{235}U as a function of axial and radial location in the fuel element, with the purpose of establishing an optimum axial zoning of the fuel elements in the Monte Carlo model in ALEPH. The simplification in this MCNP model is with respect to the FTT, CR, RB, and PB regions only, the IFE and OFE being modelled with the same level of detail as in the model for HFIR cycle 400. Only half of the core is represented in the simplified model, from the midline to the top of the core, as illustrated in Fig. C.4.

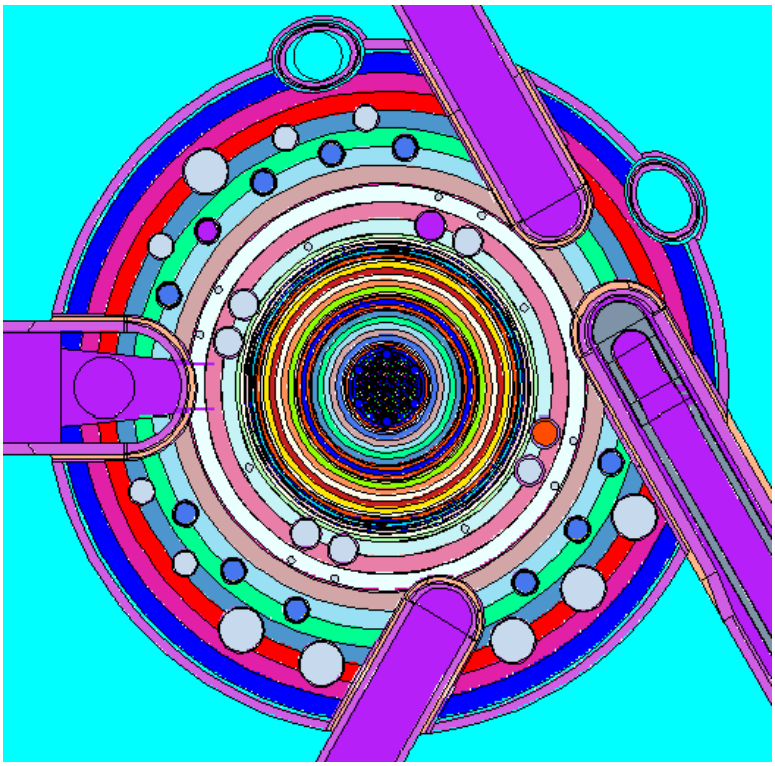

Fig. C.2. Cross section of the MCNP model for HFIR LEU at core axial midline.

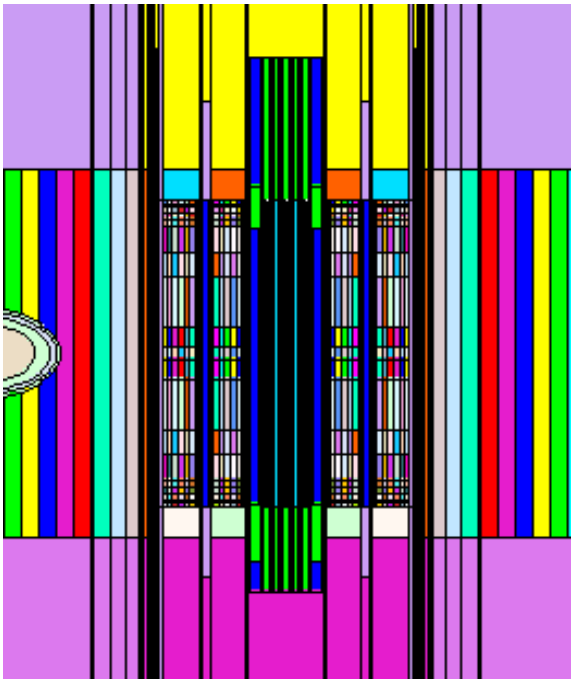

Fig. C.3. Axial cross section of the MCNP model for HFIR LEU.

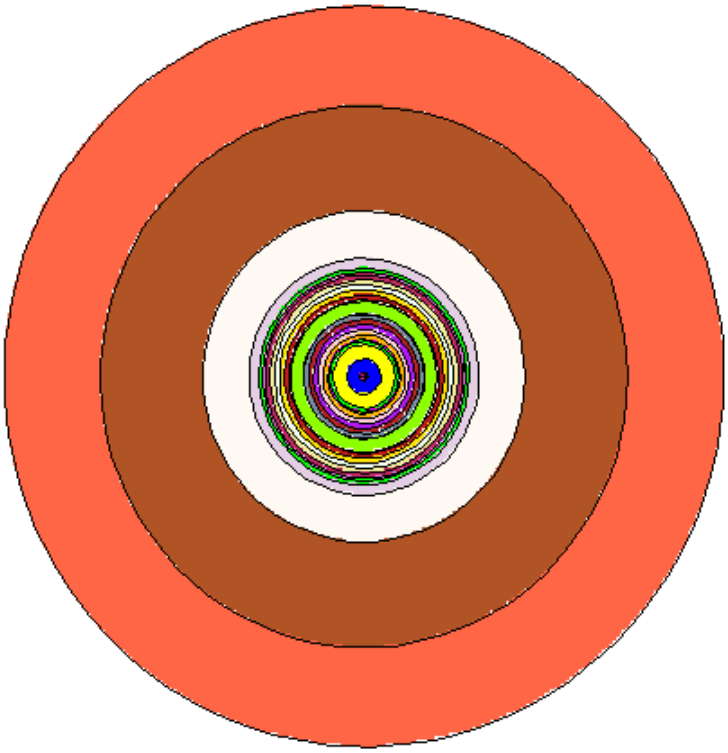

(a) radial view

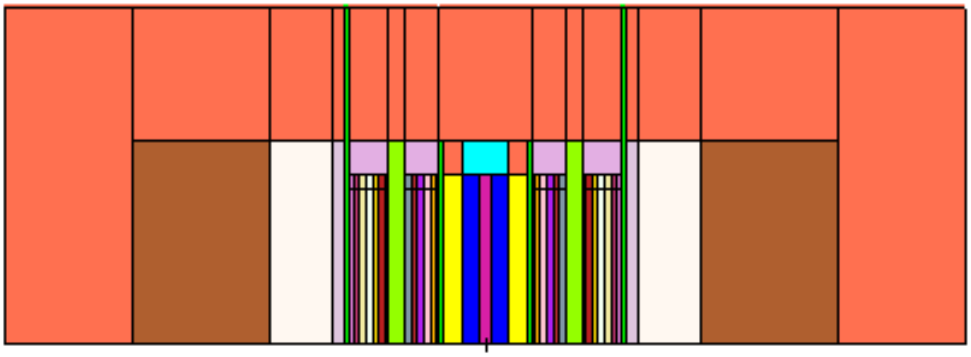

(b) axial view

Fig. C.4. 3-D MCNP simplified model for HFIR LEU.

A total of 170 tally regions are defined for the fuel elements in this MCNP model: 80 in the IFE (8 radial by 10 axial) and 90 in the OFE (9 radial by 10 axial). The thicknesses of the fuel regions in the axial direction are 0.5, 0.5, 1.0, 1.0, 1.4, 4.2, 4.2, 4.2, 4.2, and 4.2 cm from the top of the active fuel region to the core midline, for a total of 25.4 cm. The values used for the radii of the regions in the fuel elements are as shown in Table C.2.

The thermal (neutron energy < 0.625 eV) flux variation along the axial direction for a constant radius, as obtained from MCNP tallies, is shown in Figs. C.5 and C.6 for the IFE and the OFE, respectively. The radii specified in the legends for each of the radial regions are outer radii. The variations of the thermal flux as a function of radius for a constant axial location are presented in Figs. C.7 and C.8 for the IFE and OFE, respectively. The axial data (z values) shown in the legends correspond to the lower edge of each axial layer.

The variation of the thermal microscopic fission cross section for ^{235}U as a function of radial and axial location in the fuel element is presented in Figs. C.9 and C.10, respectively, for the IFE and in Figs. C.11 and C.12, respectively, for the OFE. As it can be seen from the variation of thermal flux or microscopic fission cross section for ^{235}U, the regions at the top (or bottom) edge of the fuel elements are characterized by large leakage from fuel-bearing to non-fuel-bearing regions and neutron flux spectra much different from the average flux in the fuel element.

C.2 Other Data in the ALEPH Model for HFIR LEU Core

In addition to the MCNP model of the configuration to be simulated, the input data for ALEPH includes information about the depletion mixtures (i.e., materials for which composition varies during simulation due to depletion and decay) and irradiation history. There are a total of 152 fuel regions in the IFE (8 radial by 19 axial) and 171 fuel regions (9 radial by 19 axial) in the OFE. A number of 80 depletion mixtures are specified in the IFE for the purpose of flux calculation with MCNP; as previously mentioned, this flux serves to weight the cross section data for obtaining the one-group cross sections for use in the ORIGEN 2.2 depletion calculation. From the 80 depletion mixtures in the IFE, 8 mixtures are specified in the central (i.e., core midline) axial layer of the IFE, one for each of the 8 radial regions. A unique depletion mixture is specified for fuel regions with the same radial region number and with the same axial distance with respect to the core midline; for example, if a region in the IFE is identified as IFE(r,z), where r=1,…,8 and z=1,…,19, the same depletion mixture (i.e., material number in the MCNP input file) is used in fuel regions IFE(r,1) and IFE(r,19). Similarly, there are 90 depletion mixtures in the OFE, which gives a total of 170 depletion mixtures in the fuel elements. The material in the curium targets of the central target region is also considered as a depletion mixture.

The value used for power during the irradiation was, as it will be discussed further, either 85 or 100 MW. The cross sections libraries used in the simulation were based on data from ENDF\B-VI release 8. All cross sections were considered at 300 K. As compared to the model for cycle 400, the following elements – Si, Cr, Fe, Ni, and Cu - were replaced by their isotopes from ENDF\B-VI release 8, the isotopic composition being calculated based on the natural isotopic abundances for each of these elements. The elements Mg and Ti were also replaced by their isotopes, though in these cases data from JENDL 3.3 were used because they were missing from the ENDF\B-VI.8 set.

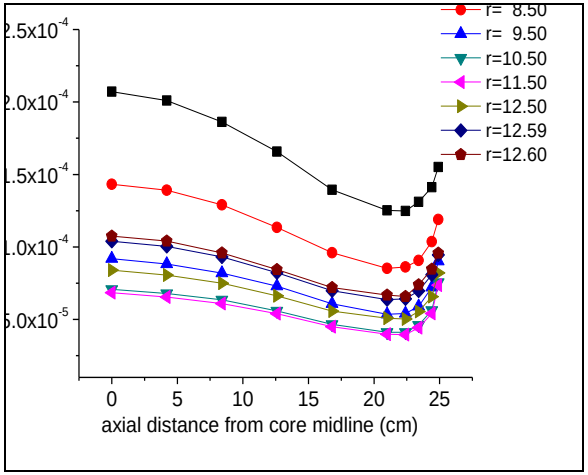

Fig. C.5. Axial variation of thermal flux in IFE.

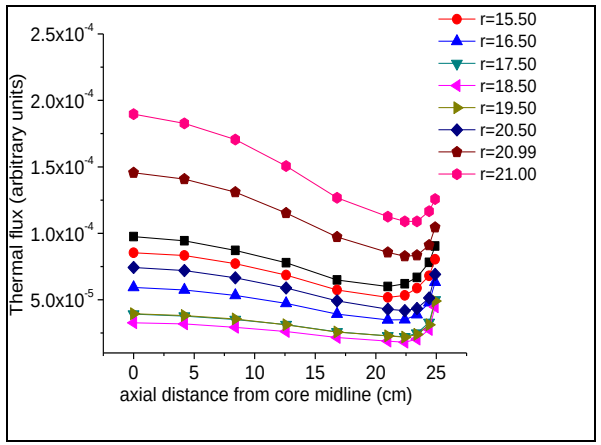

Fig. C.6. Axial variation of thermal flux in OFE.

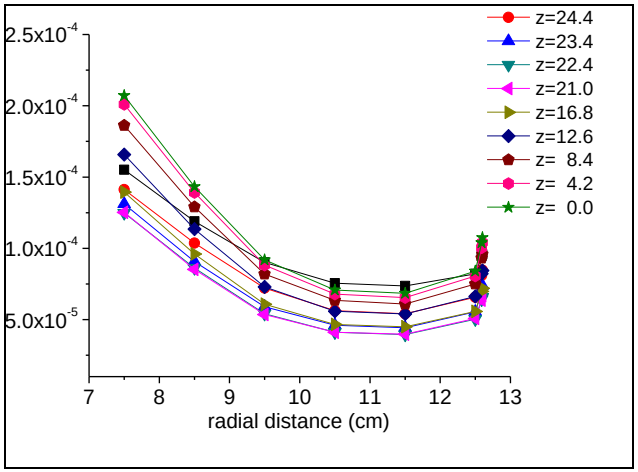

Fig. C.7. Radial variation of thermal flux in IFE.

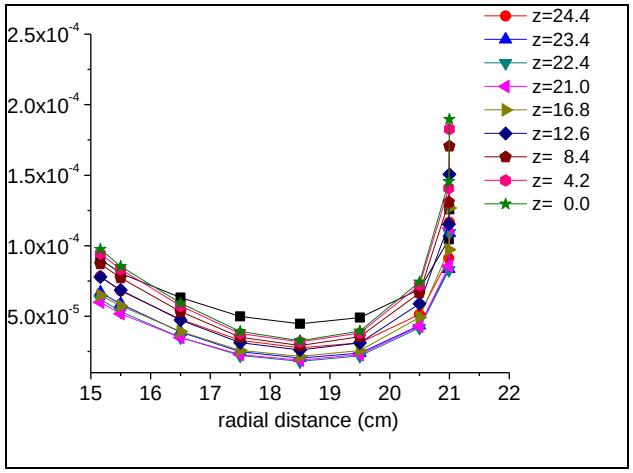

Fig. C.8. Radial variation of thermal flux in OFE.

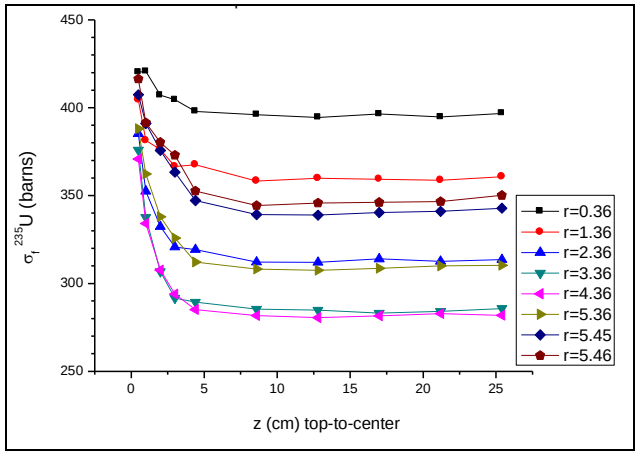

Fig. C.9. Microscopic cross section of ^{235}U vs. axial location in IFE.

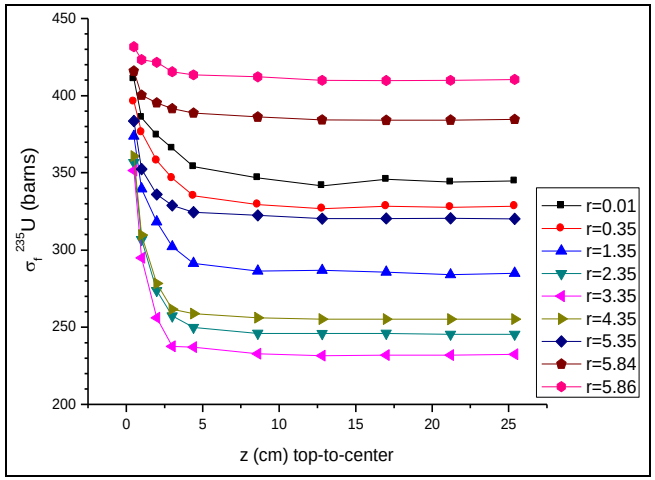

Fig. C.11. Microscopic cross section of ^{235}U vs axial location in OFE.

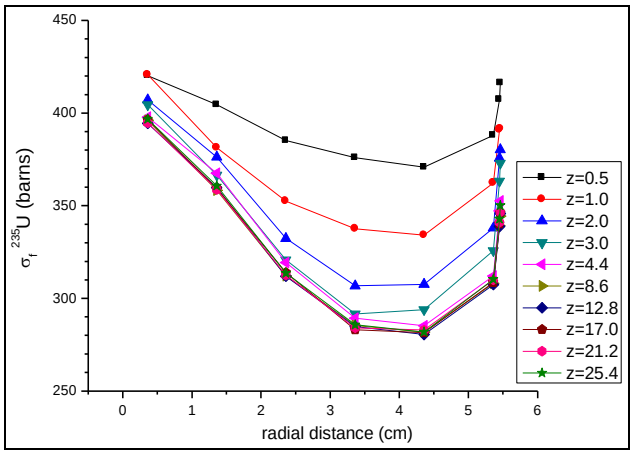

Fig. C.10. Microscopic cross section of ^{235}U vs. radial location in IFE.

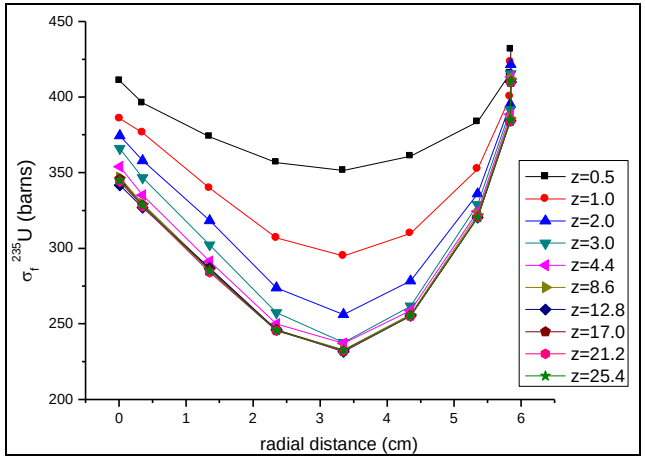

Fig. C.12. Microscopic cross section of ^{235}U vs radial location in OFE.

APPENDIX D

VARIATION OF k_{eff} AS A FUNCTION OF THE LEU FUEL LOAD

As a first step, the fuel load in the LEU model was varied with the purpose of searching for the loading that would ensure a cycle lifetime of about 26 days and performance parameters similar to those of the HFIR HEU core. Five values were considered for the ^{235}U load: 17.0, 17.9, 20.0, 25.0, and 30.5 kg. The same radial fuel grading profile was used in all these five cases, as illustrated in Fig. D.1 for the 17.9 kg load case, with no fuel grading in the axial direction. The total load of 30.5 kg is the maximum possible load (i.e., fuel meat thickness less than 0.762 mm) corresponding to this radial grading shape. For computation speed-up, the depletion simulations in all these five cases were carried out with seven depletion steps to reach a 26 days total irradiation time. The movement of the control elements during the cycle was not simulated; the control elements were considered at their fully withdrawn locations.

The variation of k_{eff} at BOC as a function of the total ^{235}U load is presented in Fig. D.2. As observed, k_{eff} variation with ^{235}U load is not linear; therefore the core lifetime (i.e., total irradiation time for which k_{eff} is greater than 1.0) is also expected to be a nonlinear function of the amount of ^{235}U in the core. The variation of k_{eff} with the irradiation time for this uncontrolled configuration and for an operating power of 85 MW is shown in Fig. D.3. As seen, a load larger than 17.9 kg as previously considered would be required to reach a cycle lifetime around 26 days. From the data shown, a 25 kg load would ensure a k_{eff} value of 1.008 at 26 days.

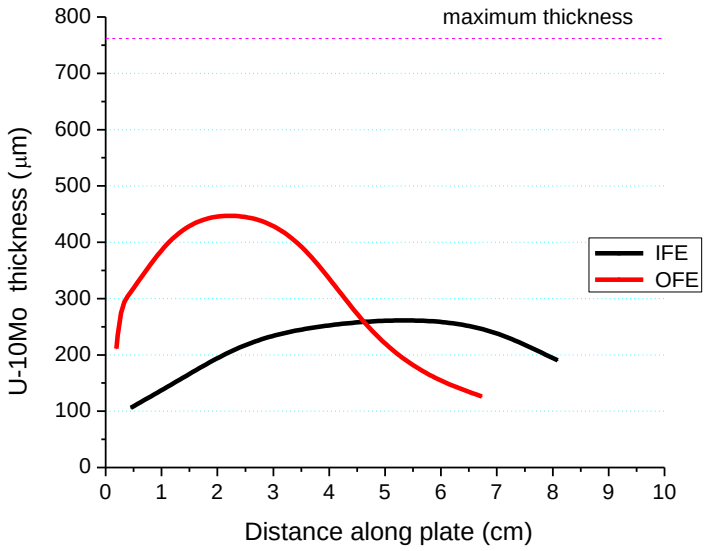

Fig. D.1. Fuel element plate profiles for 17.9 kg ^{235}U load.

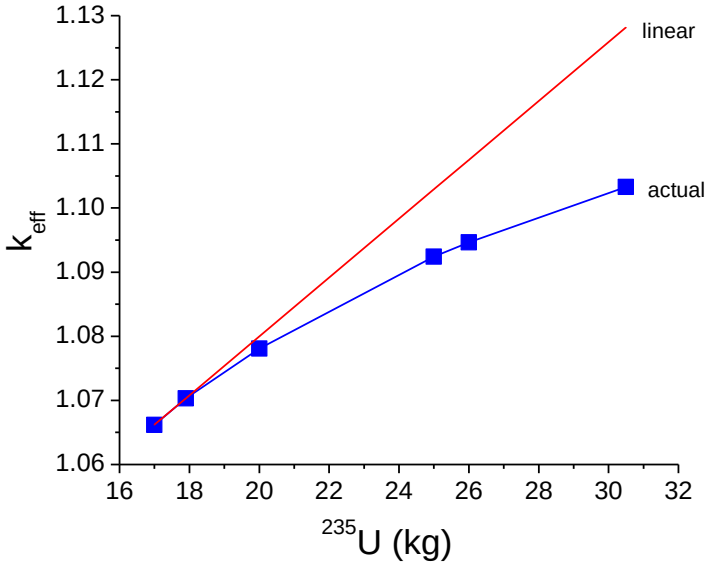

Fig. D.2. Effective multiplication constant at BOC vs. ^{235}U load.

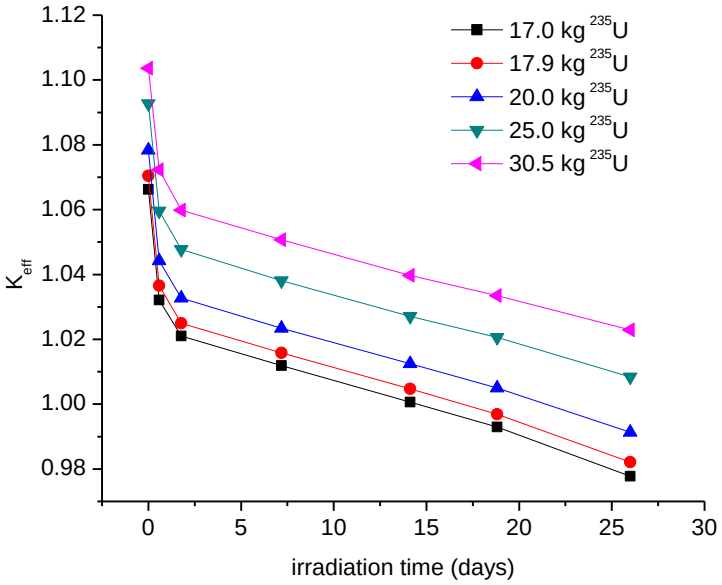

Fig. D.3. Effective multiplication constant during irradiation.

APPENDIX E

SEARCH FOR AN OPTIMUM LENGTH FOR THE AXIALLY GRADED ZONE

E.1 Three cm Axially Graded Zone

Iterative reactor core physics/thermal hydraulics calculations were performed to search for an optimum core configuration that would ensure a core performance similar to that existent for the currently operating HFIR HEU core. Iterations were carried out on both total ^{235}U load and radial fuel grading profile by searching around the 25 kg value for the total ^{235}U load. Depletion simulations with ALEPH were performed for a thermal power of 100 MW and by including in the model the movement of the control elements during the irradiation cycle. The first iterations were carried out for various profiles of the radial grading only. Axial grading was included later.

At this time, the results of the optimization study showed as a promising candidate a core with a total ^{235}U load of 25.3 kg with a radial fuel grading profile as listed in Table E.1 and illustrated in Fig. E.1. Axial grading was first applied only to the bottom 3 cm of the fuel elements, based on the observation that, as the water coolant enters the top of the core and flows from top to the bottom of the core, the occurrence of a power "spike" at the bottom of the fuel elements would be more problematic than one at the top of fuel elements and therefore this occurrence should be the first thing to be avoided. The concentration of ^{235}U in the bottom 3 cm of the fuel elements was considered to be half of the value used in the rest of the axial regions of the fuel elements.

Table E.1. Radial grading for the 25.3 kg ^{235}U core load

Inner fuel element		**Outer fuel element**	
Radial region #	Fuel meat thickness (mm)	Radial region #	Fuel meat thickness (mm)
1	0.093	1	0.217
2	0.163	2	0.266
3	0.295	3	0.432
4	0.429	4	0.639
5	0.448	5	0.633
6	0.298	6	0.533
7	0.208	7	0.396
8	0.195	8	0.215
		9	0.160

The results of the optimization performed to the current time are encouraging, though there is more work to be done before all the details of an optimum configuration will be established. The variation of the k_{eff} during the irradiation cycle is shown in Fig. E.2 for a depletion simulation with 25 depletion steps; the length of depletion steps and the location of control elements for each depletion step were the same as used for the HFIR HEU cycle 400 simulation with ALEPH. The value estimated for k_{eff} at 24.3 days of irradiation is 0.9963±0.0001. For comparison, k_{eff} at 24.3 days for the HFIR HEU cycle simulation was 0.9990±0.0002.

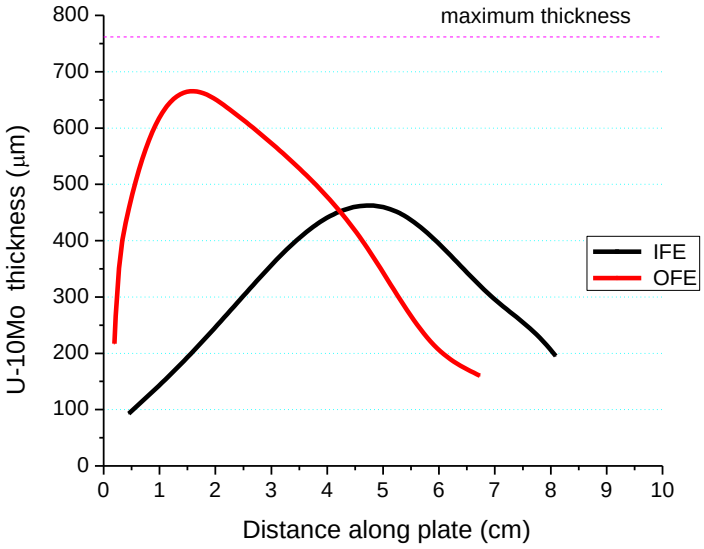

Fig. E.1. Fuel element plate profiles for 25.3 kg ^{235}U load.

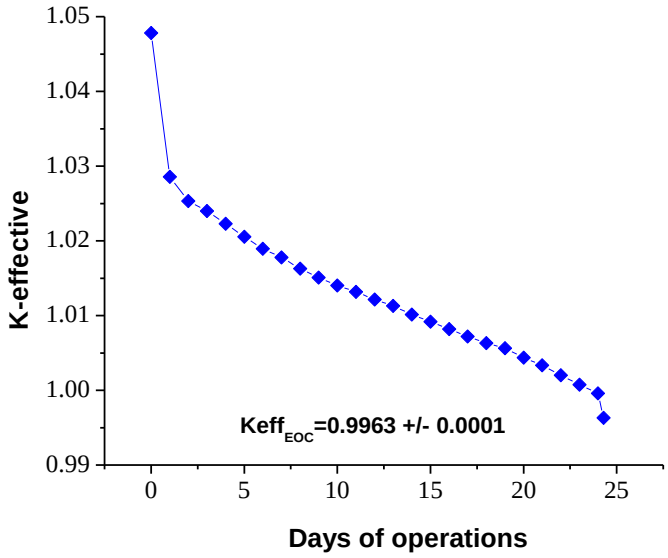

Fig. E.2. Variation of k_{eff} for 25.3 kg ^{235}U load.

The relative fission density for each of the defined regions in the fuel elements was calculated based on flux and fission density tallies in MCNP for both BOC and EOC (at 24.3 days), as shown in Tables E.2 and E.3. These data served as input for the thermal-hydraulic analysis, which estimated an operating power of 103 MW for BOC and 100.5 MW for EOC.

One of the requirements for search and optimization of an LEU core configuration is that the impact of the fuel change on the core performance and operation is minimal. The neutron flux is one of the key parameters to characterize the core performance. A comparison of the flux data for the HEU core at 85MW power and the studied LEU core at 100MW power is presented in Tables E.4 and E.5 for the BOC and EOC, respectively. The energy structure for the three-group data shown is: thermal <0.625 eV; epithermal 0.625eV-100keV; fast 100keV-20MeV. As the flux tallies provided by MCNP are normalized to the source (i.e., 1 neutron), the values for the flux in n/cm^2s were obtained by multiplying the tally values by the total source. The total source strength was *S* was approximated as shown in Appendix B of this report. For 85 MW power, the total source is $6.42x10^{18}$ n/s, and for 100 MW power is $7.56\ x10^{18}$ n/s. The comparison of the nuclide inventory data at EOC for HEU cycle 400 core and the studied LEU core, for important actinides and fission products, is presented in Table E.6.

E.2 Two Centimeter And One Centimeter Axially Graded Zones

In addition to the axial grading discussed above, two other cases were considered, in which the width of the graded axial layer at the bottom of the fuel elements was changed from 3 cm to 2 cm and 1 cm, respectively. In each of these two cases, the distribution of the relative power was calculated for BOC (see Tables E.7 and E.8) and used in thermal-hydraulic analyses. The result was that both cases were insignificantly different from the 3 cm axial grading case. This would indicate that the decision on tapering the bottom end of the fuel plates becomes a fabrication issue, decided by minimizing the cost of manufacturing.

Table E.2. Relative fission density in IFE and OFE at BOC [a]

Axial	Inner fuel element								Outer fuel element								
region #	r=1	r=2	r=3	r=4	r=5	r=6	r=7	r=8	r=1	r=2	r=3	r=4	r=5	r=6	r=7	r=8	r=9
1	0.993	1.220	1.449	1.596	1.552	1.273	1.144	1.130	1.175	1.216	1.310	1.368	1.209	1.050	0.857	0.598	0.516
2	0.862	0.955	0.983	0.982	0.979	0.944	0.965	0.961	0.999	0.974	0.894	0.806	0.698	0.646	0.615	0.519	0.476
3	0.798	0.825	0.778	0.758	0.767	0.792	0.841	0.848	0.859	0.839	0.741	0.644	0.550	0.522	0.542	0.503	0.475
4	0.778	0.782	0.716	0.700	0.722	0.738	0.778	0.783	0.781	0.772	0.697	0.620	0.532	0.510	0.545	0.527	0.500
5	0.789	0.799	0.740	0.734	0.753	0.752	0.772	0.771	0.775	0.772	0.724	0.660	0.569	0.546	0.589	0.572	0.544
6	0.899	0.915	0.858	0.860	0.883	0.858	0.863	0.862	0.863	0.870	0.839	0.785	0.682	0.660	0.718	0.694	0.663
7	1.091	1.113	1.046	1.047	1.078	1.039	1.039	1.034	1.028	1.046	1.024	0.973	0.853	0.840	0.940	0.936	0.897
8	1.292	1.319	1.243	1.250	1.287	1.247	1.244	1.238	1.236	1.258	1.238	1.185	1.056	1.070	1.276	1.348	1.320
9	1.387	1.416	1.338	1.346	1.388	1.343	1.338	1.333	1.337	1.362	1.338	1.285	1.152	1.174	1.420	1.519	1.494
10	1.393	1.421	1.343	1.356	1.398	1.353	1.350	1.346	1.344	1.363	1.344	1.293	1.158	1.181	1.428	1.524	1.503
11	1.375	1.404	1.328	1.337	1.378	1.328	1.325	1.318	1.321	1.345	1.325	1.270	1.136	1.160	1.403	1.500	1.477
12	1.250	1.278	1.201	1.208	1.242	1.199	1.193	1.189	1.195	1.214	1.190	1.135	1.009	1.015	1.196	1.251	1.221
13	1.026	1.049	0.984	0.982	1.007	0.974	0.973	0.969	0.963	0.980	0.953	0.899	0.781	0.757	0.821	0.787	0.745
14	0.846	0.857	0.798	0.796	0.817	0.798	0.804	0.804	0.801	0.809	0.773	0.715	0.617	0.590	0.632	0.599	0.564
15	0.775	0.801	0.755	0.747	0.765	0.757	0.769	0.769	0.772	0.770	0.727	0.656	0.559	0.522	0.534	0.484	0.449
16	0.419	0.471	0.484	0.492	0.501	0.470	0.443	0.437	0.440	0.463	0.471	0.432	0.357	0.326	0.304	0.233	0.199
17	0.445	0.526	0.576	0.596	0.602	0.540	0.499	0.488	0.497	0.525	0.548	0.509	0.420	0.371	0.309	0.205	0.164
18	0.481	0.602	0.704	0.761	0.750	0.636	0.560	0.551	0.560	0.602	0.659	0.639	0.534	0.454	0.342	0.199	0.154
19	0.533	0.715	0.926	1.066	1.034	0.789	0.641	0.621	0.645	0.707	0.855	0.921	0.784	0.632	0.427	0.222	0.161

[a] For the case with 25.3 kg ^{235}U loading and axial grading at the bottom 3 cm of the fuel elements.

Table E.3. Relative fission density in IFE and OFE at EOC [a]

Axial region #	Inner fuel element								Outer fuel element								
	r=1	r=2	r=3	r=4	r=5	r=6	r=7	r=8	r=1	r=2	r=3	r=4	r=5	r=6	r=7	r=8	r=9
1	0.733	1.078	1.437	1.634	1.598	1.291	1.098	1.103	1.146	1.203	1.444	1.631	1.568	1.540	1.510	1.213	1.086
2	0.698	0.939	1.070	1.063	1.060	0.996	0.953	0.969	1.008	1.007	0.996	0.938	0.864	0.909	1.076	1.050	0.998
3	0.672	0.845	0.853	0.810	0.819	0.834	0.842	0.863	0.887	0.857	0.801	0.715	0.642	0.687	0.901	0.966	0.944
4	0.656	0.799	0.785	0.739	0.750	0.761	0.777	0.800	0.809	0.783	0.740	0.672	0.607	0.644	0.850	0.931	0.919
5	0.663	0.808	0.788	0.755	0.768	0.755	0.748	0.770	0.784	0.770	0.752	0.706	0.633	0.665	0.870	0.942	0.926
6	0.724	0.905	0.900	0.863	0.874	0.840	0.818	0.843	0.858	0.835	0.836	0.808	0.729	0.761	0.968	1.005	0.978
7	0.802	1.044	1.061	1.018	1.027	0.970	0.935	0.973	0.980	0.958	0.976	0.947	0.856	0.891	1.108	1.098	1.052
8	0.860	1.169	1.232	1.183	1.185	1.109	1.056	1.103	1.120	1.085	1.117	1.089	0.982	1.024	1.256	1.202	1.143
9	0.877	1.223	1.309	1.250	1.260	1.171	1.110	1.156	1.180	1.142	1.181	1.149	1.037	1.081	1.321	1.250	1.184
10	0.877	1.229	1.315	1.256	1.257	1.174	1.115	1.165	1.182	1.141	1.188	1.156	1.042	1.090	1.329	1.252	1.180
11	0.868	1.216	1.303	1.245	1.245	1.162	1.102	1.157	1.169	1.132	1.177	1.146	1.035	1.076	1.315	1.244	1.173
12	0.844	1.148	1.209	1.157	1.163	1.089	1.038	1.083	1.099	1.065	1.100	1.069	0.964	1.005	1.235	1.188	1.129
13	0.782	1.016	1.036	0.992	0.996	0.940	0.908	0.944	0.955	0.931	0.948	0.921	0.830	0.867	1.081	1.072	1.024
14	0.714	0.887	0.875	0.836	0.850	0.817	0.802	0.823	0.842	0.820	0.814	0.780	0.703	0.735	0.941	0.981	0.959
15	0.693	0.871	0.868	0.826	0.844	0.828	0.813	0.839	0.844	0.831	0.810	0.755	0.679	0.723	0.930	0.976	0.950
16	0.369	0.502	0.572	0.570	0.572	0.523	0.475	0.468	0.484	0.501	0.541	0.515	0.467	0.505	0.613	0.564	0.516
17	0.383	0.550	0.676	0.708	0.704	0.613	0.538	0.534	0.540	0.573	0.642	0.636	0.586	0.621	0.702	0.606	0.542
18	0.393	0.593	0.798	0.888	0.872	0.711	0.595	0.587	0.608	0.657	0.780	0.838	0.784	0.802	0.821	0.658	0.572
19	0.401	0.633	0.942	1.141	1.123	0.835	0.655	0.640	0.668	0.749	0.991	1.208	1.157	1.119	1.017	0.725	0.615

[a] For the case with 25.3 kg ^{235}U loading and axial grading at the bottom 3 cm of the fuel elements.

Table E.4. Neutron flux at BOC – comparison of HEU cycle 400 and LEU cores

Location	Fuel	Thermal flux (n/cm^2s)	Epithermal flux (n/cm^2s)	Fast flux (n/cm^2s)
Central target	HEU LEU	2.2×10^{15} 2.3×10^{15}	1.3×10^{15} 1.2×10^{15}	1.1×10^{15} 1.0×10^{15}
Cold source edge	HEU LEU	6.8×10^{14} 8.1×10^{14}	2.4×10^{14} 2.8×10^{14}	9.0×10^{13} 1.0×10^{14}
Reflector r=27cm	HEU LEU	6.0×10^{14} 7.0×10^{14}	6.5×10^{14} 7.7×10^{14}	4.1×10^{14} 4.8×10^{14}

Table E.5. Neutron flux at EOC – comparison of HEU cycle 400 and LEU cores

Location	Fuel	Thermal flux (n/cm^2s)	Epithermal flux (n/cm^2s)	Fast flux (n/cm^2s)
Central target	HEU LEU	2.3×10^{15} 2.5×10^{15}	1.1×10^{15} 1.2×10^{15}	9.9×10^{14} 1.0×10^{15}
Cold source edge	HEU LEU	8.3×10^{14} 8.3×10^{14}	2.4×10^{14} 2.7×10^{14}	8.9×10^{13} 9.9×10^{13}
Reflector r=27cm	HEU LEU	8.1×10^{14} 7.2×10^{14}	6.5×10^{14} 7.3×10^{14}	4.0×10^{14} 4.5×10^{14}

Table E.6. EOC inventory data for HEU and LEU cores

Nuclide	HEU cycle 400 core (g)	LEU core (g)
B-10	0.203	0.746
B-11	12.480	10.280
Kr-86	15.840	18.140
Zr-93	53.480	61.840
Mo-97	51.440	60.220
Tc-99	43.580	51.620
Ru-101	46.950	55.670
Ru-103	24.280	29.860
Rh-103	5.121	6.466
Rh-105	0.530	0.989
I-135	1.263	1.357
Xe-131	18.640	22.660
Xe-133	23.270	27.860
Xe-135	0.054	0.271
Cs-133	50.180	60.310
Cs-134	1.531	1.266
Cs-135	2.910	12.290
Ce-141	58.760	68.790
Pr-143	40.940	48.120
Nd-143	26.340	32.160
Nd-145	49.380	58.250
Nd-147	14.060	17.450
Pm-147	11.960	15.390
Pm-148	0.257	0.257
Pm-148m	0.088	0.151
Pm-149	2.059	2.403
Sm-149	0.382	1.876
Sm-150	13.200	14.080
Sm-151	1.133	3.329
Sm-152	7.005	7.147
Sm-153	0.646	0.618
U-234	88.040	232.100
U-235	6785.000	22250.000
U-236	502.300	740.300
U-238	532.000	101700.000
Np-237	6.188	9.369
Np-238	0.134	0.121
Np-239	2.777	76.170
Pu-238	0.273	0.624
Pu-239	11.410	390.900
Pu-240	1.429	25.440
Pu-241	0.612	8.070
Pu-242	0.049	2.799

Table E.7. Relative fission density in IFE and OFE at BOC [a] for 1-cm axial grading

Axial	Inner fuel element								Outer fuel element								
region #	r=1	r=2	r=3	r=4	r=5	r=6	r=7	r=8	r=1	r=2	r=3	r=4	r=5	r=6	r=7	r=8	r=9
1	0.981	1.209	1.441	1.596	1.540	1.260	1.130	1.118	1.160	1.201	1.307	1.372	1.207	1.046	0.849	0.598	0.507
2	0.860	0.945	0.971	0.976	0.969	0.934	0.950	0.951	0.973	0.958	0.890	0.808	0.695	0.642	0.610	0.517	0.475
3	0.792	0.818	0.773	0.752	0.764	0.782	0.831	0.835	0.854	0.832	0.737	0.640	0.546	0.514	0.538	0.503	0.472
4	0.769	0.773	0.712	0.697	0.715	0.731	0.760	0.771	0.781	0.767	0.696	0.618	0.526	0.503	0.541	0.519	0.496
5	0.782	0.787	0.731	0.727	0.751	0.747	0.763	0.757	0.768	0.770	0.714	0.652	0.563	0.539	0.581	0.563	0.536
6	0.890	0.908	0.850	0.852	0.875	0.852	0.855	0.852	0.850	0.858	0.830	0.779	0.674	0.651	0.710	0.686	0.655
7	1.077	1.104	1.037	1.037	1.068	1.032	1.032	1.027	1.027	1.041	1.015	0.965	0.845	0.831	0.928	0.924	0.889
8	1.286	1.315	1.236	1.243	1.279	1.238	1.234	1.231	1.231	1.250	1.227	1.173	1.046	1.058	1.267	1.340	1.313
9	1.381	1.413	1.330	1.339	1.381	1.335	1.330	1.315	1.326	1.352	1.328	1.279	1.142	1.167	1.413	1.510	1.483
10	1.391	1.423	1.338	1.349	1.388	1.341	1.341	1.334	1.331	1.355	1.337	1.282	1.147	1.172	1.420	1.518	1.493
11	1.378	1.400	1.320	1.327	1.369	1.321	1.318	1.312	1.313	1.337	1.317	1.267	1.134	1.154	1.393	1.494	1.469
12	1.252	1.279	1.202	1.210	1.245	1.201	1.199	1.196	1.194	1.214	1.189	1.137	1.008	1.014	1.193	1.246	1.219
13	1.032	1.054	0.984	0.987	1.013	0.977	0.971	0.967	0.963	0.981	0.958	0.903	0.784	0.759	0.819	0.785	0.742
14	0.845	0.857	0.799	0.795	0.818	0.794	0.800	0.800	0.796	0.802	0.773	0.719	0.616	0.590	0.630	0.596	0.565
15	0.745	0.751	0.686	0.677	0.697	0.697	0.717	0.717	0.720	0.717	0.667	0.598	0.508	0.481	0.500	0.461	0.436
16	0.737	0.742	0.688	0.668	0.687	0.702	0.730	0.737	0.733	0.731	0.658	0.572	0.484	0.445	0.438	0.385	0.350
17	0.779	0.838	0.820	0.813	0.817	0.805	0.824	0.823	0.838	0.830	0.766	0.673	0.563	0.500	0.439	0.326	0.280
18	0.451	0.548	0.622	0.659	0.648	0.560	0.508	0.500	0.523	0.547	0.573	0.550	0.462	0.388	0.295	0.176	0.137
19	0.514	0.679	0.866	0.993	0.965	0.735	0.601	0.581	0.611	0.670	0.801	0.861	0.727	0.585	0.397	0.207	0.153

Table E.8. Relative fission density in IFE and OFE at BOC [a] for 2-cm axial grading

Axial region #	Inner fuel element								Outer fuel element								
	r=1	r=2	r=3	r=4	r=5	r=6	r=7	r=8	r=1	r=2	r=3	r=4	r=5	r=6	r=7	r=8	r=9
1	0.986	1.216	1.442	1.589	1.553	1.269	1.139	1.135	1.171	1.206	1.309	1.367	1.201	1.044	0.851	0.596	0.511
2	0.868	0.963	0.980	0.985	0.974	0.937	0.950	0.949	0.976	0.965	0.896	0.804	0.693	0.648	0.614	0.519	0.477
3	0.797	0.826	0.775	0.762	0.765	0.792	0.836	0.845	0.847	0.835	0.740	0.641	0.544	0.520	0.540	0.503	0.478
4	0.766	0.778	0.714	0.700	0.719	0.733	0.782	0.791	0.781	0.772	0.702	0.620	0.531	0.508	0.544	0.525	0.497
5	0.784	0.795	0.736	0.728	0.748	0.746	0.772	0.766	0.767	0.776	0.719	0.660	0.568	0.545	0.589	0.570	0.544
6	0.890	0.908	0.852	0.855	0.882	0.856	0.856	0.854	0.850	0.863	0.833	0.781	0.682	0.661	0.715	0.692	0.660
7	1.084	1.105	1.040	1.044	1.072	1.035	1.028	1.027	1.027	1.044	1.020	0.968	0.850	0.836	0.935	0.932	0.895
8	1.286	1.312	1.235	1.245	1.284	1.240	1.239	1.233	1.234	1.254	1.233	1.176	1.049	1.064	1.271	1.346	1.319
9	1.392	1.417	1.336	1.344	1.386	1.341	1.336	1.333	1.339	1.360	1.335	1.280	1.147	1.167	1.413	1.514	1.489
10	1.389	1.422	1.344	1.351	1.388	1.346	1.334	1.330	1.339	1.368	1.343	1.282	1.152	1.173	1.419	1.523	1.500
11	1.369	1.402	1.319	1.329	1.371	1.330	1.330	1.323	1.321	1.347	1.321	1.267	1.134	1.156	1.399	1.493	1.469
12	1.251	1.277	1.203	1.207	1.243	1.201	1.194	1.192	1.193	1.213	1.190	1.137	1.009	1.015	1.197	1.250	1.218
13	1.028	1.049	0.984	0.986	1.008	0.971	0.969	0.967	0.969	0.984	0.957	0.902	0.786	0.759	0.822	0.788	0.744
14	0.846	0.859	0.799	0.796	0.813	0.794	0.798	0.800	0.799	0.805	0.770	0.717	0.618	0.591	0.632	0.600	0.562
15	0.755	0.765	0.703	0.693	0.710	0.709	0.732	0.730	0.735	0.733	0.678	0.608	0.517	0.490	0.506	0.467	0.440
16	0.769	0.800	0.760	0.749	0.768	0.765	0.777	0.774	0.780	0.777	0.724	0.644	0.539	0.496	0.473	0.400	0.366
17	0.430	0.494	0.529	0.548	0.551	0.504	0.473	0.464	0.473	0.492	0.503	0.463	0.381	0.336	0.282	0.192	0.157
18	0.475	0.586	0.680	0.734	0.731	0.616	0.553	0.538	0.546	0.586	0.636	0.624	0.516	0.440	0.333	0.195	0.149
19	0.527	0.703	0.911	1.043	1.015	0.774	0.639	0.616	0.632	0.696	0.837	0.907	0.767	0.617	0.421	0.218	0.160

(This page blank)

Appendix F
New cross section processing methodology

The cross section processing methodology used previously[19, 20] for the 1-D fuel grading studies is based on a set of modules in SCALE that perform resonance processing (BONAMI, NITAWL) and 1-D transport calculations (XSDRNPM) based on a radial representation of the core, resulting in relatively large errors in power density near the top and bottom of the fuel elements. A new cross section processing methodology aims to insure a more appropriate representation of the cross section data for the fuel regions located near the axial edges of the fuel element.

The new methodology is based on the TRITON/NEWT sequence - newly available in SCALE - that allows 2-D depletion calculations for arbitrary-mesh geometries. The two-dimensional cross section processing approach provides a better representation of the spatial dependence of the neutron flux, especially important for the fuel regions at the top and bottom of the fuel elements. These regions are characterized by large leakage from fuel-bearing to non-fuel bearing regions and neutron flux spectra much different than the average flux in the fuel element. Since coolant flow in HFIR is axial - top to bottom - improving the results of the BOLD-VENTURE calculation also improves the accuracy of the thermal hydraulic analysis of the reactor core. The thermal safety margins for HEU fuel in HFIR were demonstrated by measurement but assessment of LEU fuel performance must be by computational models as suitable test facilities no longer exist in the U.S. While 2-D models for cross section processing have been in common use in the power reactor industry for decades, the recently-developed, "freely available", arbitrary-mesh geometry was needed for 2-D cross section processing for HFIR due to the HFIR fuel being in the form of involute-shaped plates rather than a lattice of fuel pins.

Simplified, 1-D, consistent models of HFIR for use among the XSDRNPM, NEWT, VENTURE, and MCNP codes were developed as a first approximation of the new 2-D methodology and to facilitate a comparison with the previously methodology based on XSDRNPM. Consistency checks were carried out for the collapsed cross sections obtained with NEWT with the 1-D model by direct comparison to corresponding data obtained with the 1-D transport code XSRNPM in SCALE, for which microscopic cross section collapsing and formatting is available. It was found that the microscopic cross section data agree well, including the transport cross sections though a new estimation algorithm had to be implemented in NEWT different from that encoded in version 5.1 of SCALE. The maximum difference between collapsed cross section values was 5% which occurred in the transport cross section for hydrogen in the coolant. Note that the comparison is between one-dimensional models not a test of the "absolute" accuracy of the cross section values as could be obtained, for instance, by comparison to MCNP-derived cross sections.

Both NEWT and XSDRNPM models provide values of the multiplication constant, k_{eff}, that are in very good agreement with the corresponding MCNP value (difference less than 0.08%). The use of 20-group microscopic cross section data obtained from XSDRNPM in BOLD VENTURE provides a k_{eff} in good agreement with both MCNP (0.12%) and XSDRNPM (0.04%). The use with BOLD VENTURE of collapsed cross section data obtained from the 1-D NEWT model provides results similar to those obtained with XSDRNPM-based cross sections.

A 2-D NEWT model was developed to calculate few-group cross sections. Consistent, simplified 3-D HFIR models (relative to the model described in [19]) were developed for both BOLD VENTURE and MCNP to allow comparison of reactor parameters without post-calculation processing of code results. Continuous energy cross section data was used for MCNP whereas NEWT calculations employed a 238-group SCALE transport library. Both cross section data were based on ENDF/B-V nuclear data files. The 2-D NEWT model of HFIR represents an axial cross section of the reactor core that cuts the annular core into two equal halves. Due to symmetry, only one quarter of the axial cut is modeled, as illustrated in Fig. F.1. Reflective boundary conditions are imposed on the left and bottom of the bounding surfaces, and white boundary conditions on the other two edges of the configuration. The geometry and material composition data is consistent to that used in the 3-D MCNP detailed model of HFIR developed by Xoubi and Primm and in the BOLD VENTURE model of HFIR used for 1-D grading studies[15, 16]. However, no control plates or irradiation targets are included in the NEWT model. The fuel radial grading is modeled in detail, as used in the 1-D grading study for LEU fuel [2]. For the purpose of cross section collapsing, for each fuel region with unique material composition data, multiple zones are specified on the axial direction. For each of the zones, NEWT calculates a zone-averaged flux that is used to collapse the 238-group SCALE master library data to a few-group structure. Therefore, the effect of axial flux variation is included in the resulting microscopic cross sections as compared to the fuel element axially-uniform flux that is inherent in the 1-D cross section processing methodology.

As a preliminary verification, the spatial variation across fuel elements of relevant four-group macroscopic cross sections and fluxes obtained with the NEWT model was compared to the corresponding results obtained with the similar, simplified, 3-D Monte Carlo (MCNP) transport model. For cross section comparison, six tally regions were defined in a fuel element: three radial by two axial. In the radial directions, three zones were defined, one corresponding to the mid radial zone of the fuel element and the other two to the radial edges. In the axial direction, two zones were defined, one for the top 2 cm of the element, and the other for the rest of the axial direction to the core midline.

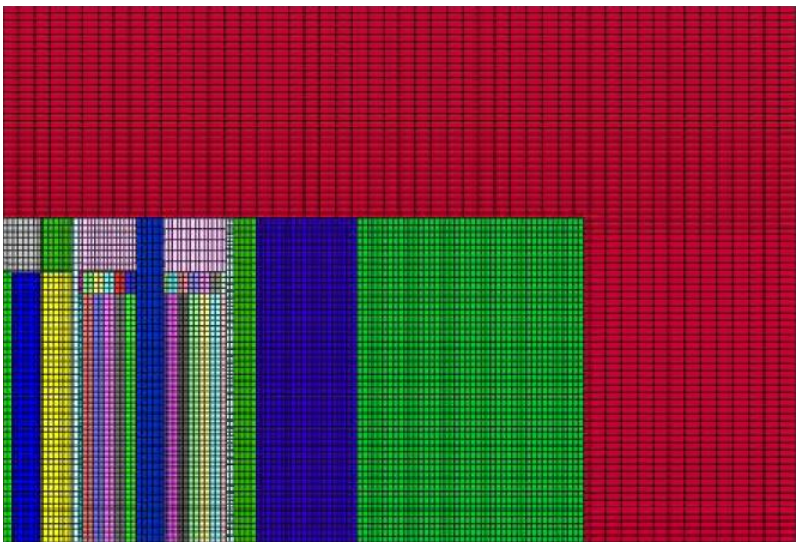

Fig. F.1. 2-D NEWT model of HFIR for cross section generation.

Appendix G
Assessment of accuracy of new data processing methodology

Calculated k_{eff} for the cross section data processing code, NEWT, was compared to results from the HFIR MCNP HEU model. Good agreement was observed for the k_{eff} values which were 1.0862 (σ=0.0003) for MCNP and 1.0780 for NEWT, the difference being about 0.6%. The maximum difference between the two methods for the macroscopic fission cross section over the thermal energy range for the spatial elements considered was 3%. The good agreement of the results showed that the transport solutions obtained with the two models are consistent. However, it could not provide information about the transport cross section comparison, as tallying this type of cross section is not available in the standard MCNP code.

Further testing of the NEWT-based cross section processing methodology was carried out for a HFIR LEU-fuelled configuration. The model is simplified, as compared to the real configuration, of the control element and target region, but maintains the representation of the fuel grading as defined in the so-called real configuration. The grading profile for the LEU fuel corresponds to one of the cases described in ref. 19. The zoning of the fuel regions is similar to that presented in the previous section, but the widths of the axial layers are a little different in this case, with values of 0.5, 0.5, 1.0, 1.0, 1.4, 4.2, 4.2, 8.2, 3.2, and 1.0 cm from top of the active fuel region to the core midline. Consistent 3-D MCNP, 2-D NEWT, and 3-D BOLD-VENTURE models were developed for this simplified HFIR configuration. Multigroup microscopic cross sections were generated with the NEWT model for all nuclides in the problem for each of the 170 fuel zones. A SCALE 238-group neutron transport cross section library was used in the NEWT calculation. The flux resulted from the transport calculation was used to collapse the cross section data to a 20-group structure as shown in Table G.1 below.

The 20-group cross section data were used in diffusion calculations with the BOLD-VENTURE model (R-Z geometry). The VENTURE-calculated k-effective was 1.083. The value from the 3-D full-detail MCNP for the corresponding model was 1.070. The power density data obtained from BOLD-VENTURE was compared to the fission density profile obtained from the MCNP calculation. As expected, differences in power are larger in the fuel zones at the edges of the fuel elements (inner radial edge in IFE and top axial edge in IFE and OFE) that are characterized by large leakage and where the diffusion theory approximation may not be accurate. The differences in power density are illustrated in Figs. G.1 and G.2 for the IFE and OFE, respectively, as a function of the radial and axial regions. The radial regions are numbered from 1 to 8 for the IFE and from 1 to 9 for the OFE with increasing radius; the axial regions are numbered from 1 to 10 with increasing axial location from core midline (0 cm) to 25.4 cm, which is the top of the active fuel region.

The largest differences, of about 10%, are observed for the fuel zones at the top left corner of the IFE. For the innermost radial edge of the IFE the difference decreases axially from 10% at the top to less than 3% at the core midline. In the case of the IFE, the difference generally decreases with increasing radius for a constant axial location, with the exception of the outermost radial regions of the IFE that are close to the core midline. Note that the axial layers 7-10 with larger differences correspond to the top 3 cm of the fuel element.

In the case of the OFE, the largest differences are seen in the top axial layer, of up to 7%, and at the innermost radial layer, of up to 6%. The differences in the few top layers in the OFE case are a few percent smaller than the corresponding data for the IFE. Note that the differences in those regions of the OFE in which most of the core power is generated (top axial layers and edge radial layers excluded) are less than 3%. This level of agreement (maximum error of ~ 10%) is a significant improvement over the previous

method's results and approaches that needed for design evaluations (a value of 5% would correspond to the level of uncertainty in measurements of local reactor physics parameters for the current, HEU fuel, i.e. at 5%, the level of agreement among computational methods would correspond to the standard deviation in measured, local physics parameters for the current, HEU fuel).

The 2-D cross section processing methodology proves to be promising, as indicated by the results obtained. There is a significant improvement, as compared to a currently-used 1-D cross section processing methodology, with respect to the power distribution calculated with BOLD-VENTURE, especially for the fuel regions located at the edges of the fuel elements. This result is of particular importance, as a better representation of the power distribution would propagate in a more accurate thermal-hydraulics analysis of the core where the power data are used and consequently in a better estimation of core safety parameters.

Table G.1
Energy structure for collapsing from 238- to 20-group

20-group #	238-group #	Lower energy (eV)
1	12	2.48×10^{6}
2	15	1.50×10^{6}
3	25	8.75×10^{5}
4	45	8.50×10^{4}
5	63	2.58×10^{3}
6	86	9.00×10^{1}
7	116	2.75×10^{1}
8	132	9.10×10^{0}
9	149	2.97×10^{0}
10	163	1.68×10^{0}
11	190	9.75×10^{-1}
12	199	6.25×10^{-1}
13	205	3.75×10^{-1}
14	210	2.50×10^{-1}
15	215	1.25×10^{-1}
16	222	4.00×10^{-2}
17	226	7.50×10^{-3}
18	230	2.50×10^{-3}
19	232	1.50×10^{-3}
20	238	1.00×10^{-5}

As previously mentioned, the studied configuration for cross section processing is a simplified model of the HFIR. However, it is considered an appropriate model for a proof of principle and for facilitating the estimation of the effect of various uncertainties in the modeling parameters on the results obtained. Going from simpler to complex, more configuration details would need to be included in the current model for a better approximation of the actual core configuration. For example, the control plates region between the two fuel elements will be included in the NEWT model.

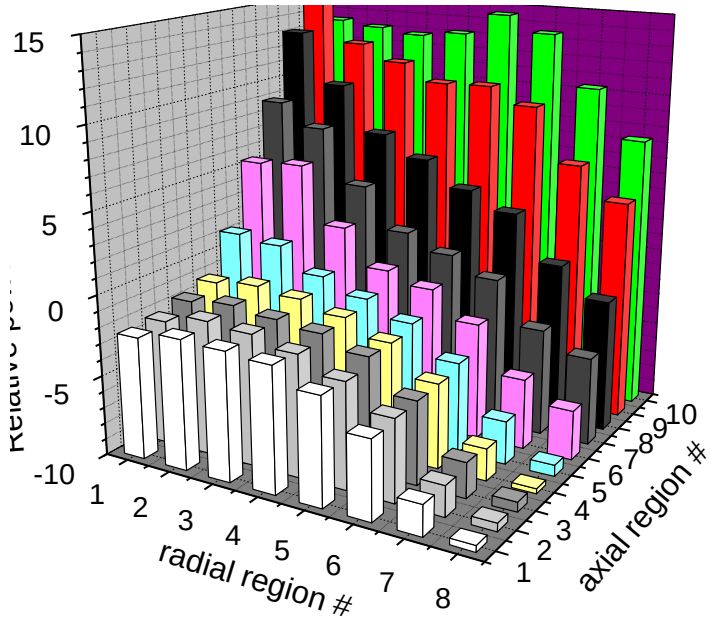

Fig. G.1. Difference in relative power for the inner fuel element.

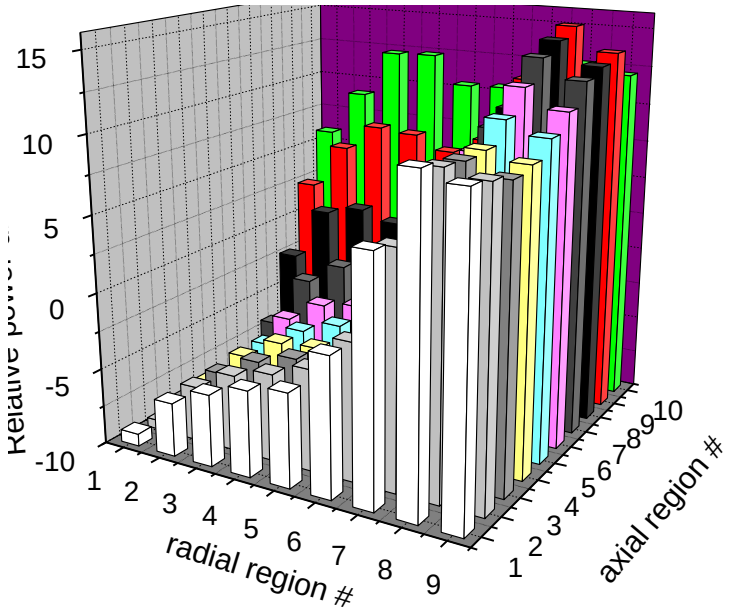

Fig. G.2. Difference in relative power for the OFE.

(This page blank)

INTERNAL DISTRIBUTION

1. S. T. Baker (*bakerst@ornl.gov*)
2. K. J. Beierschmitt (*beierschmitt@ornl.gov*)
3. J. L. Binder *(binderjl@ornl.gov*)
4. C. A. Blue (*blueca@ornl.gov*)
5. S. E. Burnette (*burnettese@ornl.gov*)
6. C. W. Coates (*coatescw@ornl.gov*)
7. B. S. Cowell (*cowellbs@ornl.gov*)
8. D. C. Christensen (*christensend@ornl.gov*)
9. R. A. Crone (*cronera@ornl.gov*)
10. R. J. Ellis (*ellisrj@ornl.gov*)
11. J. C. Gehin (*gehinjc@ornl.gov*)
12. G. Ilas (*ilasg@ornl.gov*)
13. J. H. Miller (*millerjh2@ornl.gov*)
14. L. J. Ott (*ottlj@ornl.gov*)
15. C. V. Parks (*parkscv@ornl.gov)*
16–18. R. T. Primm III (*primmrtiii@ornl.gov*)
19. R. R. Rawl (*rawlrr@ornl.gov*)
20. A. W. Riedy (*riedyaw@ornl.gov*)
21. J. E. Rushton (*rushtonje@ornl.gov*)
22. L. J. Satkowiak (*satkowiaklj@ornl.gov*)
23. J. D. Sease (*seasejd@ornl.gov*)
24. K. A. Smith (*smithka@ornl.gov*)
25. R. L. Snipes (*snipesrl@ornl.gov*)
26. C. C. Southmayd (*southmaydcc@ornl.gov*)
27. S. J. Zinkle (*zinklesj@ornl.gov*)
28. ORNL Laboratory Records (*hamrindr@ornl.gov*)

EXTERNAL DISTRIBUTION

29. A. Adams, U.S. Nuclear Regulatory Commission, One White Flint North, 11555 Rockville Pike, Rockville, Maryland 20852-2738 (*axa@nrc.gov*)
30. T. Andes, BWXT/Y-12, Y-12 National Security Complex, P.O. Box 2009, Oak Ridge, TN 37831-8245 (*andestc@y12.doe.gov*)
31. R. A. Butler, Director, Research Reactor Center, 1513 Research Park Drive, Columbia, MO 65211 (*ButlerRa@missouri.edu*)
32. G. S. Chang, Idaho National Laboratory, P.O. Box 1625, Idaho Falls, ID 83415-3885 (*gray.chang@inl.gov*)
33. D. Chong, NA-212, U.S. Department of Energy, 1000 Independence Avenue SW, Washington, DC 20585 (*Daniel.Chong@nnse.doe.gov*)
34. H. E. Clark, U.S. Department of Energy Oak Ridge Office, P.O. Box 2001, Oak Ridge, TN 37831 (*hkc@ornl.gov*)
35. D. Diamond, Brookhaven National Laboratory, P.O. Box 5000, Upton, NY 11973-5000 (*diamond@bnl.gov*)
36. C. Galvez, 637 NW 14th Street, Corvallis, OR 97330 (*galvezc@berkeley.edu*)
37. H. D. Gougar, Manager, Fission & Fusion Systems, INEEL, P.O. Box 1625, MS 3860, Idaho Falls, ID 83415-3860 (*goughd@inl.gov*)
38. M. Hassler, BWXT/Y-12, Y-12 National Security Complex, P.O. Box 2009, Oak Ridge, TN 37831-8245 (*hasslerme@y12.doe.gov*)
39. M. Hutmaker, U.S. Department of Energy, 1000 Independence Avenue SW, Washington, DC 20585 (*matthew.hutmaker@nuclear.energy.gov*)
40. D. Kutikkad, Assistant Reactor Manager-Physics, University of Missouri Research Reactor Facility, Columbia, MO 65211 (*kutikkadk@missouri.edu*)
41. J. Matos, Argonne National Laboratory, 9700 S. Cass Avenue, Argonne, IL 60439 (*jim.matos@anl.gov*)
42. C. McKibben, University of Missouri Research Reactor Facility, Columbia, MO 65211 (*mckibben@missouri.edu*)
43. D. M. Meyer, Idaho National Laboratory, P.O. Box 1625, Idaho Falls, ID 83415-3750 (*Dana.Meyer@inl.gov*)
44. T. Newton, MIT Nuclear Reactor Laboratory, 138 Albany St., Cambridge, MA 02139 (*tnewton@mit.edu*)
45. W. Richards, NIST Center for Neutron Research, 100 Bureau Drive, Stop 8561, Gaithersburg, MD 20899-8561 (*wade.richards@nist.gov*)

46. W. C. Richardson, BWXT Technology, Inc., 2016 Mount Athos Rd., Lynchburg, VA 24504 (*WCRichardson@bwxt.com*)
47. J. Roglans, Argonne National Laboratory, 9700 S. Cass Avenue, Argonne, IL 60439 (*roglans@anl.gov*)
48. J. Snelgrove, Argonne National Laboratory, 9700 S. Cass Avenue, Argonne, IL 60439 (*jimsnelgrove@anl.gov*)
49. P. Staples, NA-212, U.S. Department of Energy, 1000 Independence Avenue SW, Washington, DC 20585 (*Parrish.Staples@nnsa.doe.gov*)
50. Daniel M. Wachs, MFC 791 B-147, Idaho National Laboratory, P.O. Box 6188, Idaho Falls, ID 83415 (*Daniel.Wachs@inl.gov*)
51. R. E. Williams, NIST Center for Neutron Research, 100 Bureau Drive, Stop 8560, Gaithersburg, MD 20899-8560 (*robert.williams@nist.gov*)